Published in final edited form as:
Cell Rep. 2022 November 15; 41(7): 111649. doi:10.1016/j.celrep.2022.111649.

Developmental spontaneous activity promotes formation of sensory domains, frequency tuning and proper gain in central auditory circuits

Calvin J. Kersbergen[1], **Travis A. Babola**[1], **Jason Rock**[2], **Dwight E. Bergles**[1,3,4,5,*]

[1]The Solomon H. Snyder Department of Neuroscience, Johns Hopkins University, Baltimore, MD, USA

[2]Genentech, Inc., San Francisco, CA, USA

[3]Department of Otolaryngology-Head and Neck Surgery, Johns Hopkins University, Baltimore, MD, USA

[4]Kavli Neuroscience Discovery Institute, Johns Hopkins University, Baltimore, MD, USA

[5]Lead contact

SUMMARY

Neurons that process sensory information exhibit bursts of electrical activity during development, providing early training to circuits that will later encode similar features of the external world. In the mammalian auditory system, this intrinsically generated activity emerges from the cochlea prior to hearing onset, but its role in maturation of auditory circuitry remains poorly understood. We show that selective suppression of cochlear supporting cell spontaneous activity disrupts patterned burst firing of central auditory neurons without affecting cell survival or acoustic thresholds. However, neurons in the inferior colliculus of these mice exhibit enhanced acoustic sensitivity and broader frequency tuning, resulting in wider isofrequency laminae. Despite this enhanced neural responsiveness, total tone-responsive regions in the auditory cortex are substantially smaller. Thus, disruption of pre-hearing cochlear activity causes profound changes in neural encoding of sound, with important implications for restoration of hearing in individuals who experience reduced activity during this critical developmental period.

In brief

Kersbergen et al. show that correlated firing of auditory neurons prior to hearing onset requires supporting cell excitation of cochlear hair cells via TMEM16A. Selective genetic disruption of

---

[*]Correspondence: dbergles@jhmi.edu.

AUTHOR CONTRIBUTIONS
C.J.K., conceptualization, methodology, investigation, formal analysis, funding acquisition, and writing – original draft; TAB, methodology, investigation, formal analysis, writing – review & editing; J.R., tools and reagents and writing – review & editing; D.E.B., conceptualization, methodology, supervision, funding acquisition, writing – original draft, and writing – review & editing.

DECLARATION OF INTERESTS
D.E.B. is a paid consultant of Decibel Therapeutics.

SUPPLEMENTAL INFORMATION
Supplemental information can be found online at https://doi.org/10.1016/j.celrep.2022.111649.

pre-hearing spontaneous activity led to enhanced sensitivity of auditory neurons to sound, broader frequency tuning, and spatial compression of brain auditory centers.

Graphical Abstract

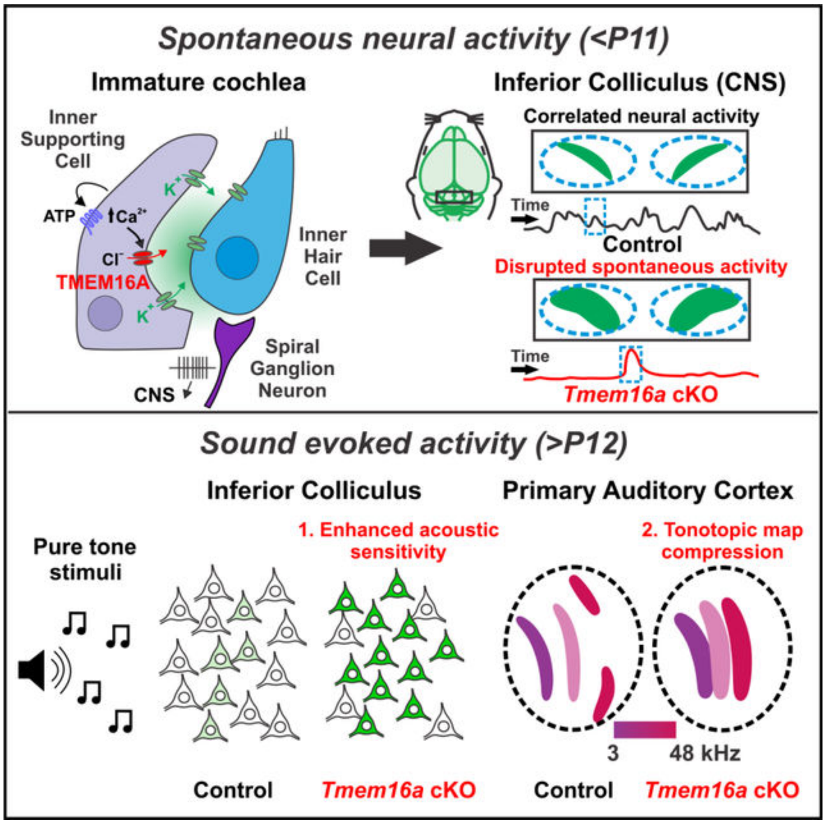

INTRODUCTION

Acoustic information is processed in discrete auditory centers of the brain to enable verbal communication, discrimination, and sound localization. The features of acoustic stimuli necessary to interpret sounds, such as frequency (pitch) and sound pressure (loudness), can be extracted from the earliest detectable sound input (Kandler et al., 2009; Babola et al., 2018), indicating that core features of auditory neural pathways are established prior to sensory experience. Before onset of hearing, neurons in nascent sound processing networks experience periodic bouts of spontaneous electrical activity resembling future activation to pure-tone acoustic stimuli (Lippe, 1994; Tritsch et al., 2007; Sonntag et al., 2009; Babola et al., 2018), providing the means to promote survival of neurons in nascent auditory centers, initiate their maturation, and refine their connections through activity-dependent processes (Katz and Shatz, 1996; Kirkby et al., 2013; Martini et al., 2021). However, the role of this early patterned activity in stimulating functional maturation of auditory circuits is poorly understood because of the inability to selectively disrupt this activity while preserving cochlear function to allow later assessment of sound processing capabilities of neurons in the brain.

Auditory neuron burst firing is initiated peripherally in the developing cochlea when ATP is released by inner supporting cells (ISCs), which together form a transient epithelium, known as Kölliker's organ, that lies adjacent to inner hair cells (IHCs). The resulting activation of purinergic P2RY1 autoreceptors on ISCs initiates a cascade of events, culminating in chloride efflux through TMEM16A (ANO-1) calcium-activated chloride channels, which draws potassium ions out of these cells to induce depolarization of nearby IHCs, triggering glutamate release and eventually burst firing of spiral ganglion neurons (SGNs) (Tritsch et al., 2007, 2010; Wang et al., 2015). During this pre-hearing period, projections from medial olivocochlear neurons form synapses on immature IHCs, providing efferent feedback to regulate precise burst firing patterns and bilateral representation of neural activity in the developing CNS (Clause et al., 2014; Wang et al., 2021). Although ATP release from cochlear supporting cells is stochastic and variable, it is highly effective at inducing transient, spatially restricted activation of IHCs along the length of the cochlea. Therefore, spontaneous events initiated in the cochlea during this period resemble future activation to pure-tone acoustic stimuli and propagate through nascent sound processing circuits to reach the auditory cortex, providing a means to reinforce connections between neurons along tonotopic boundaries throughout the auditory system (Babola et al., 2018). However, spontaneous activity engages many of the same components used later for sound transduction. Manipulations that disrupt spontaneous activity by targeting these cells and components during development also result in loss of trophic support, efferent silencing, neuronal degeneration, and deafness, limiting functional *in vivo* interrogation of the auditory pathway to define the precise roles of pre-hearing spontaneous activity (Tierney et al., 1997; Mostafapour et al., 2000; McKay and Oleskevich, 2007; Noh et al., 2010; Clause et al., 2014; Tong et al., 2015). These studies suggest that even modest alterations in spontaneous activity can disrupt the tonotopic precision of connectivity and tuning properties of central auditory neurons (Clause et al., 2014, 2017; Müller et al., 2019; Maul et al., 2022).

To assess the role of this early patterned activity in the functional maturation of sound processing networks, we selectively disrupted expression of TMEM16A channels in ISCs and performed *in vivo* imaging of spontaneous and sound-evoked neural activity in awake mice. Loss of cochlear TMEM16A channels suppressed pre-hearing neuronal calcium transients in the inferior colliculus (IC) and disturbed normally precise, tonotopically restricted activation patterns that occur at this age. These animals exhibited normal cochlear structure and no cellular degeneration or hearing loss after ear canal opening (approximately postnatal day 12 [P12]), allowing assessment of spatial and temporal features of sound-evoked neural activity in central auditory centers. *In vivo* imaging of neuronal calcium transients in the IC of these mice revealed that neuronal responses to pure tones were larger in amplitude and that more neurons were activated by a given stimulus, indicative of abnormally high gain. Neurons responded to a broader range of frequencies, and the spatial map of responding neurons was wider, indicating that sharp tonotopic portioning of acoustic information was not achieved. Macroscopic imaging revealed compression of the midbrain tonotopic map and that cortical regions involved in processing tonal stimuli were substantially smaller. These results demonstrate that intrinsically generated bursts of activity that emerge from the developing cochlea are required to establish appropriate sensitivity to incoming acoustic information and consolidate regions of the brain devoted to processing sound.

RESULTS

TMEM16A channels are required for spontaneous activity prior to hearing onset

Opening of TMEM16A channels in ISCs results in profound chloride efflux, inducing a concomitant efflux of potassium ions that depolarizes nearby IHCs (Wang et al., 2015; Figure 1A). Our previous studies indicated that genetic inactivation of *Tmem16a* abolished most spontaneous activity in IHCs and reduced SGN burst firing. However, the *Pax2-Cre* mouse line used to inactivate *Tmem16a* exhibits incomplete recombination in the cochlea and widespread expression outside of the inner ear (Wang et al., 2015). To determine whether ISC-generated spontaneous activity requires TMEM16A throughout postnatal development, we crossed *Tmem16a*$^{fl/fl}$ mice with *Tecta-Cre* mice, which exhibit recombination in the sensory epithelium of the embryonic cochlea with limited recombination in other central auditory nuclei (Babola et al., 2020, 2021; Figures 1B and S1). ISCs in *Tmem16a* conditional knockout (cKO) mice exhibited no spontaneous inward currents during whole-cell patch-clamp recordings throughout postnatal, pre-hearing development (Figures 1C, 1D, and S2A–S2E) but retained their low membrane resistance (Figures S2F and S2G), indicative of retained gap junction coupling. ISCs did not exhibit spontaneous osmotic crenations (Tritsch et al., 2007), which are induced by TMEM16A-mediated chloride efflux (Wang et al., 2015; Figures S2H and S2I).

Consistent with the critical role of TMEM16A in inducing local extracellular potassium transients, IHCs in P7 cochleae of *Tmem16a* cKO mice no longer exhibited slow inward currents that induce calcium action potentials (Beutner and Moser, 2001; Tritsch et al., 2010; Johnson et al., 2011; Figures 1E and 1F), leaving only infrequent efferent synaptic responses (Glowatzki and Fuchs, 2000; Figure 1E, asterisks and inset). *Tmem16a* cKO mice exhibited spontaneous calcium transients in IHCs (Figures 1G and 1H); however, these transients were no longer coordinated among neighboring IHCs and exhibited reduced amplitudes (Figures 1H and 1I). Calcium transients in *Tmem16a* cKO IHCs no longer correlated with local ISC calcium activity (Figures S3E–S3H; Video S1). These isolated IHC calcium events arise from tonic IHC depolarization because of accumulation of extracellular potassium around IHCs when TMEM16A-mediated osmotic crenation is prevented (Babola et al., 2020; Figures S4A–S4D). This phenotype recapitulates IHC behavior in mice in which ATP-dependent activation of ISCs was prevented (Babola et al., 2020, 2021). Similarly, SGNs in *Tmem16a* KO mice exhibit altered firing patterns, including near elimination of long burst events and prolongation of inter-spike intervals (Wang et al., 2015). A recent report suggested that TMEM16A enhances ATP release through positive feedback mechanisms in the cochlea (Maul et al., 2022); however, we observed no significant change in the frequency, amplitude, duration, or area of calcium transients in ISCs of *Tmem16a* cKO mice (Figures S3A–S3D; Video S1), in accordance with prior observations (Wang et al., 2015). These results indicate that TMEM16A is required to induce periodic, coordinated activation of IHCs throughout the postnatal pre-hearing period, providing a means to selectively disrupt spontaneous activity in the auditory system during this crucial period of development.

Deletion of *Tmem16a* suppresses burst firing of central auditory neurons prior to hearing onset

ISC-induced depolarization of IHCs triggers excitation of SGNs, leading to discrete bursts of action potentials that propagate throughout the central auditory system (Sonntag et al., 2009; Tritsch et al., 2010; Clause et al., 2014). Each ATP release event results in coordinated IHC activation in a restricted region of the cochlea, enabling correlated firing of neurons within isofrequency laminae that will ultimately process similar frequencies of sound. To determine how disruption of TMEM16A-induced ionic flux in the cochlea influences spontaneous activity patterns of central auditory neurons *in vivo*, we performed macroscopic imaging of the IC in awake, unanesthetized mice expressing the genetically encoded calcium indicator GCaMP6s in neurons (*Snap25-T2A-GCaMP6s*) (Madisen et al., 2015; Figure 2A). In control mice (*Tmem16a*$^{fl/fl}$;*Snap25-T2A-GCaMP6s*, P7), neurons within isofrequency laminae exhibited periodic calcium increases, resulting in spatially restricted bands of activity mirrored across the IC (Babola et al., 2018; Wang et al., 2021; Figure 2B, events 1–4). Spontaneous activity of auditory neurons was dramatically disrupted in *Tmem16a* cKO mice, with fewer calcium transients detected in the IC (Figures 2C and 2D; Video S2). Residual activity in these mice consisted of low-amplitude, brief events (Figure 2C, events 1 and 2) interspersed with large-amplitude, long-duration events occurring approximately once every 2 min that were no longer confined to narrow isofrequency boundaries and displayed high correlation between IC lobes (Figures 2C and 2D, events 3 and 4). These changes in activity are reflected in the histogram of event amplitudes (Figure 2E) and cumulative distribution of durations (Figure 2F), with *Tmem16a* cKO mice exhibiting shifts toward the distribution extremes for both parameters. Analysis of fluorescence changes across the tonotopic axis revealed that spontaneous events in *Tmem16a* cKO mice resulted in broader activation of neurons (Figures 2G–2I) with a significant increase in mean spatial activation (e.g., bandwidth) (control, 250.0 ± 25.4 μm; cKO, 325.6 ± 41.4 μm; $p = 0.002$, two-sample t test; $n = 6$ and 8 mice, respectively). Spatial widening of spontaneous events was not driven only by large-amplitude transients in *Tmem16a* cKO mice; analysis of calcium transients along the tonotopic axis with a peak fluorescence of less than 20% also revealed increased spatial activation (Figures S5A–S5C), indicating that loss of cochlear TMEM16A expression disrupts the precise patterning of correlated neuronal calcium activity in isofrequency laminae. Retina-induced spontaneous waves of neuronal activity in the superior colliculus (Ackman et al., 2012) did not exhibit changes in frequency or duration in *Tmem16a* cKO mice (Figure S6), suggesting that cochlear deletion of *Tmem16a* did not induce global physiological changes in the CNS.

In vivo two-photon imaging of spontaneous neural activity in the IC at this age confirmed that activity patterns observed during wide-field imaging arise from local neuronal activity (including projections) and not light scattering from other brain regions. Automated grid-based analyses revealed that IC neurons in *Tmem16a* cKO mice exhibited significantly fewer correlated events, but when they occurred, they typically encompassed a much larger portion of the IC (Figures S5D–S5H). To determine whether these changes in IC spontaneous activity patterns occur throughout the pre-hearing period, we performed wide-field imaging from mice aged P10–P11, just prior to ear canal opening (Mikaelian and Ruben, 1965; Geal-Dor et al., 1993; Anthwal and Thompson, 2016). *Tmem16a* cKO mice at this age continued to exhibit reduced activity and dramatic increases in the amplitude and spatial width of residual spontaneous events (Figure S7), consistent with previous studies indicating that the cochlea uses a similar mechanism to induce spontaneous activity throughout early development (Tritsch and Bergles, 2010; Babola et al., 2021). These results show that disruption of ion flux from ISCs alters the normal spatial and temporal patterning of spontaneous neural activity in the central auditory system prior to hearing onset.

Cochlear structure and acoustic sensitivity are preserved in *Tmem16a* cKO mice

To determine how pre-hearing spontaneous activity influences the functional organization of central auditory centers, the ability of the cochlea to transduce acoustic stimuli must be intact after knockout of *Tmem16a*. To determine whether developmental deletion of *Tmem16a* alters cochlear structure or cell survival, we performed histological assessments of *Tmem16a* cKO cochleae at P14, just after hearing onset, and at P21, when mice exhibit normal hearing thresholds. No changes in gross structure of the cochlea, organ of Corti, or tectorial membrane were observed in these mice (Figure 3A), and no degeneration of hair cells or SGNs was evident across the length of the cochlea at P14 or P21 (Figures 3B–3E and S8A–S8F). To determine whether the ability to transduce acoustic stimuli is intact in mice with disrupted spontaneous activity, we measured auditory brainstem responses (ABRs) at P14 and P21. Auditory thresholds to click and pure-tone stimuli were unaltered in *Tmem16a* cKO mice (Figures 3F, 3G, and S8G–S8I), although subtle differences in ABR waveforms were evident, including a slightly lower amplitude (Figure 3H) and longer latency of wave 1 and subsequent waveforms (Figure 3I), suggesting that SGN activation may be slightly less synchronous. These results indicate that the cochlea retains the ability to transduce acoustic information to the CNS despite disruption of spontaneous activity prior to hearing onset.

Disruption of pre-hearing spontaneous activity enhances the gain of central auditory neurons in awake mice

To determine how auditory neurons in the CNS respond to sound when deprived of patterned spontaneous activity prior to hearing onset, we assessed sound-evoked neural activity in the IC just after ear canal opening (P13–P15), using wide-field imaging of GCaMP6s in awake, unanesthetized mice (Figure 4A). In control and *Tmem16a* cKO mice, presentation of pure tones to the left ear elicited broad regions of neural activity in both lobes of the IC that were aligned to diagonally oriented isofrequency domains, with the strongest response observed in the contralateral IC (Babola et al., 2018; Figure 4B). Low-frequency tones elicited a single band of activity in the central portion of the IC, whereas higher-frequency tones elicited dual bands in more lateral regions (Figure 4B), following the known spatial segregation of frequency information in the IC (Stiebler and Ehret, 1985; Barnstedt et al., 2015; Wong and Borst, 2019). Control and *Tmem16a* cKO mice exhibited similar response thresholds (Figures 4C and 4D), in accordance with ABR measurements (Figure 3G), indicating that core aspects of auditory encoding remain intact. However, *Tmem16a* cKO mice exhibited several anomalies, including a marked increase in the amplitude of sound-evoked responses to a given sound intensity, particularly to suprathreshold tones above 3 kHz (Figures 4E and 4F). This increase in gain was accompanied by a widening of the area responsive to individual tones (e.g., bandwidth) along the dorsal tonotopic axis across a range of frequencies and sound intensities (Figures 4G, 4H, and S9A–S9J), resulting in increased overlap of pure-tone isofrequency laminae.

Neurons display increased gain and broader frequency sensitivity when deprived of spontaneous burst firing

To assess the response properties of individual auditory neurons, we performed two-photon calcium imaging in the central nucleus of the IC (Figure 5A). Neuronal somata and neuropil responsive to a given frequency exhibited markedly larger increases in calcium to tone presentation in *Tmem16a* cKO mice (Figures 5B, 5C, and S10A–S10F; Video S3), indicating that these gain changes manifest in single neurons. More neurons in each field responded to each tone (Figure 5D), demonstrating that these changes in sensitivity were pervasive in sound-responsive collicular neurons. We also determined the frequency tuning of IC neurons by measuring their response to a range of frequencies (3–24 kHz) at different sound attenuation levels (40–90-decibel [dB] sound pressure level [SPL]). Neurons in control mice exhibited sharp tuning, responding to a narrow range of frequencies, with calcium levels increasing with higher sound intensities (Figures 5E and 5F). In contrast, neurons in *Tmem16a* cKO mice exhibited much broader tuning, responding to a wider range of frequencies (Figures 5E–5H and S10G–S10I; Video S4), with a significant increase in the mean maximum bandwidth across animals (control, 0.76 ± 0.17 octaves; cKO, 1.48 ± 0.31 octaves; $p = 7.7804e{-}5$, two-sample t test, $n = 8$ and 7 mice) and exhibited larger calcium increases to their best frequency stimulus at a given sound intensity (Figures 5I and S10J). Thus, individual auditory neurons exhibit higher gain and broader tuning when deprived of spontaneous burst firing prior to hearing onset.

Spatial compression of frequency representation after disruption of developmental spontaneous activity

To determine whether spontaneous activity influences the partitioning of frequency information in the IC (i.e., the tonotopic map), we also measured the spatial segregation of tone-evoked responses across the IC, perpendicular to the isofrequency laminae (Figure 6A). The peak response location to supratheshold (100-dB SPL), pure-tone stimuli (i.e., site of best frequency) shifted from the center for low frequencies to the lateral regions of the IC for higher frequencies in control and *Tmem16a* cKO mice (Figures 6A and 6B, red and black dashed lines), indicating that gross tonotopic partitioning is maintained. However, the location of the peak response shifted significantly less with increasing frequency in *Tmem16a* cKO mice (Figures 6B and 6C); in concert with the broadening of frequency responsiveness, there was less spatial separation between frequency-responsive domains and overlapping pure-tone response regions (Figures 6A and 6D; Video S5). This macroscopic spatial compression of the tonotopic map persisted over a wide range of sound intensities (Figures S11A–S11G), suggesting that a fundamental change in frequency encoding occurs upon disruption of pre-hearing spontaneous activity. Low-magnification, two-photon imaging of neurons in the central nucleus of the IC provided further evidence of this dramatic phenomenon; a much broader distribution of frequencies at suprathreshold levels was represented in the fixed area of the imaging field (Figure 6E). Maps of neuronal best frequency (the frequency that elicits the largest calcium response) and center frequency (the frequency of calcium response at the lowest sound intensity) obtained with higher-magnification imaging revealed that individual regions of the IC contained neurons with a much wider range of best and center frequencies (Figures 6F–6I), confirming an underlying topographic organizational change beyond expansion of neuronal receptive fields. These data indicate that the area devoted to processing sound information in the IC is compressed when input from the cochlea is suppressed during the postnatal, pre-hearing period.

Neuronal activity initiated in the cochlea prior to hearing onset propagates throughout the central auditory system. However, dual IC-auditory cortex (AC) imaging revealed that approximately half of the burst events in the AC arise from non-cochlear sources, raising questions about the distinct roles of peripheral and central activity sources in shaping auditory cortical development (Siegel et al., 2012; Babola et al., 2018; Gribizis et al., 2019). To determine how disruption of spontaneous peripheral input influences later sound processing in the AC, we performed wide-field imaging of sound-evoked responses in P13–P16 mice. The AC is segregated into discrete high- and low-frequency-responsive regions, or foci, along multiple tonotopic gradients (Figure 7A, red and blue areas; Issa et al., 2014; Romero et al., 2020). Remarkably, in contrast to the enhanced gain observed in the IC, the amplitudes of neuronal responses in the primary AC (A1) were comparable in control and *Tmem16a* cKO mice after hearing onset (P13–P14) (Figures 7B and 7C). However, the spatial separation between frequencies (6–24 kHz, 80-dB SPL) was reduced (Figures 7D and 7E), with a change in the spatial representation of higher-frequency tones; rather than split into two discrete foci as seen in control mice, 24-kHz responses in *Tmem16a* cKO mice were represented by a single focus, reminiscent of frequency responses in the control A1 lower than 24-kHz (Figure 7D). Similarly, at P15–P16, the tone-responsive area of the A1 at 80-dB SPL evoked by range of frequencies (3–48 kHz) was reduced (Figures 7F and 7G), and the cumulative tone-responsive area of the AC was smaller in *Tmem16a* cKO mice (control, 3.19 mm^2; cKO, 2.77 mm^2; Figure 7H). Multiple high-frequency foci were induced in the A1 by a 48-kHz tone in older *Tmem16a* cKO mice, but the distances between the centroids of these foci and between low- and high-frequency foci in the A1 were decreased (Figures 7I and 7J), indicating macroscopic compression of sound-responsive areas in the AC. These results indicate that disruption of early patterned activity reduces the cortical territory devoted to processing tonal information.

DISCUSSION

Neurons in nascent sensory processing networks fire periodic bursts of action potentials prior to onset of sensory experience. *In vivo* measures of spontaneous activity (Sonntag et al., 2009; Clause et al., 2014; Babola et al., 2018) indicate that each auditory neuron will experience more than 30,000 discrete bursts (~2.0 bursts/min, ~2,900 bursts/day) prior to onset of hearing. This correlated activity propagates from the cochlea to the AC, mimicking aspects of stimulus encoding that may enable networks to process future sensory input (Kirkby et al., 2013; Ge et al., 2021; Tiriac et al., 2022) and providing cues for refinement of central connectivity. However, assessing the effect of this prominent, intrinsically generated activity on the functional organization of the auditory system has been difficult because permanent manipulations of the auditory system necessarily disrupt spontaneous activity and later processing of sound. Complete silencing of auditory nerve activity during the pre-hearing period through cochlear ablation or pharmacological inhibition results in dramatic circuit reorganization; however, these manipulations are accompanied by loss of trophic support and substantial neuron loss (Tierney et al., 1997; Mostafapour et al., 2000). Similarly, models of congenital deafness exhibit impaired synapse pruning, reduced axonal refinement, and disrupted tonotopic ion channel gradients in the auditory brain stem before hearing onset (Leake et al., 2006; Leao et al., 2006; Hirtz et al., 2011, 2012; Müller et al., 2019), but later deafness of these animals limits functional interrogation of auditory centers. More subtle manipulations of spontaneous activity patterns through genetic alteration of efferent feedback to the cochlea impaired refinement and maturation of medial nucleus of the trapezoid body (MNTB)-lateral superior olive (LSO) synaptic connectivity, disrupted the tonotopic gradient of electrophysiologic properties of neurons in the MNTB, increased central auditory thresholds, and impaired behavioral frequency discrimination (Clause et al., 2014, 2017; Di Guilmi et al., 2019; Wang et al., 2021); however, these mice retain dysfunctional olivocochlear feedback after hearing onset. Here we leveraged new insight into the molecular mechanisms that initiate burst firing in the developing cochlea to selectively disrupt this highly stereotyped activity in auditory centers prior to hearing onset while preserving the ability of the cochlea to transduce sound after hearing begins. We show that this developmental patterned activity is necessary to establish proper acoustic sensitivity, sharpen the frequency tuning of auditory neurons, and form future auditory responsive domains in the midbrain and cortex. These results indicate that disruption of activity patterns prior to hearing onset, with no detectable cell loss, is sufficient to induce profound developmental changes in sound processing networks.

Cochlear supporting cells induce bursts of neural activity in the developing auditory system

In the pre-hearing cochlea, supporting cells in Kölliker’s organ initiate spontaneous neural activity through release of ATP, engagement of purinergic P2RY1 receptors, and activation of TMEM16A. Pharmacologic or genetic disruption of this mechanism alters patterns of spontaneous activity in IHCs, SGNs, and neurons of the MNTB and IC, disrupting temporal firing patterns and reducing burst frequency (Wang et al., 2015; Babola et al., 2020; Maul et al., 2022). However, silencing supporting cell activity reduced, but did not eliminate, the spontaneous activity of IHCs and SGNs or block correlated firing of central auditory neurons prior to hearing onset, suggesting that there are other mechanisms that may contribute to burst firing at this age. Our prior studies indicated that loss of TMEM16A or P2RY1 causes an ~10-mV depolarizing shift in the membrane potential of IHCs because of buildup of extracellular potassium when extracellular space around these cells collapses (Wang et al., 2015; Babola et al., 2020). As a result, IHC membrane potential is near threshold, allowing these cells to generate calcium spikes with minimal stimulus, leading to spurious, spatially uncoordinated activity. This emergent IHC activity may engage central auditory neurons (Maul et al., 2022) but without the precise, spatially restricted coordination afforded by supporting cell-mediated excitation. When deprived of synaptic input, SGNs become hyperexcitable and respond directly to ISC potassium transients (Babola et al., 2018). Similar enhanced excitability may occur in neurons throughout the auditory pathway, progressively amplifying weak inputs and predisposing these circuits to paroxysmal activity, manifesting in the IC-wide events observed in *Tmem16a* cKO mice.

Gain control in developing sensory pathways

Our studies in awake mice reveal that, when deprived of prehearing burst firing, the gain of sound-evoked responses in the auditory midbrain was abnormally elevated, with higher amplitude neural responses and broader isofrequency laminae particularly evident to suprathreshold stimuli. These results suggest that nascent sound processing networks are designed to maximize initial responsiveness, in accordance with the over-production of neurons and excitatory synaptic connections, higher intrinsic excitability of neurons, and delayed maturation of inhibition in the developing brain (Scott et al., 2005; Dorrn et al., 2010; Sun et al., 2010; Wong and Marín, 2019). Early patterned activity is then used to balance excitation and inhibition in these networks to enable proper responsiveness and prevent runaway excitation at hearing onset (Vale and Sanes, 2000, 2002; Kotak et al., 2008). Similar adaptation occurs in the mature auditory system, in which attenuation of peripheral input and hearing loss triggers the gain enhancement necessary to preserve acoustic detection thresholds (Kotak et al., 2005; Auerbach et al., 2014; Chambers et al., 2016).

Although prominent in subcortical regions, neuronal responsiveness was not significantly increased in the AC, suggesting that central auditory centers rely on distinct mechanisms to refine response properties. Although burst firing in the IC is abolished by cochlear removal at P7 (Tritsch et al., 2010; Babola et al., 2018), sound processing centers in the AC receive additional excitatory drive from local cortical activity and cross-modal inputs (Siegel et al., 2012; Gribizis et al., 2019), which may enable a homeostatic reduction in excitability when deprived of peripheral auditory input. The magnitude of gain enhancement in the IC of *Tmem16a* cKO mice was highest in regions with the greatest acuity and gradually declined with decreasing stimulus frequency. Auditory circuits adapted for processing higher frequencies appear to be prone to maladaptive gain enhancement; tinnitus primarily manifests as a perception of high-pitch “ringing,” and hyperacusis is most acute at higher frequencies (Stouffer and Tyler, 1990; Gu et al., 2010; Hébert et al., 2013). Although likely important for maintaining activity levels critical for neural survival and circuit refinement, this increased gain in developing sensory pathways could prove detrimental for normal circuit function in maturity and may contribute to developmental disorders in which sensory hypersensitivity is common (Penagarikano et al., 2007; Marco et al., 2011).

Refinement of sensory receptive fields by intrinsic neural activity

Sensory neurons exhibit precise tuning to specific environmental features. This sensitivity emerges initially through axon guidance cues that establish coarse organization, followed by neural activity-dependent refinement via synapse strengthening or elimination (Katz and Shatz, 1996; Huberman et al., 2008; Dhande et al., 2011; Sitko and Goodrich, 2021). In the visual, olfactory, and somatosensory systems, early spontaneous activity has been shown to play crucial roles in refinement of sensory neuron projections and formation of receptive fields (Grubb et al., 2003; Yu et al., 2004; Chandrasekaran et al., 2005; Mrsic-Flogel et al., 2005; Burbridge et al., 2014; Che et al., 2018; Mizuno et al., 2018; Antón-Bolaños et al., 2019). Like the topographic organization of other sensory pathways, tonotopic information is processed in discrete domains throughout the auditory system, enabling isolation of frequency components critical for differentiating pitch and deconvolving complex sounds. In *Tmem16a* cKO mice, individual IC neurons displayed broader tuning, and correspondingly, the spatial representation of pure tones across the tonotopic axis in the IC was expanded, indicating that early patterned neural activity initiates functional refinement in auditory processing centers. However, it is also possible that the infrequent, large-scale events observed in *Tmem16a* cKO mice may contribute to the expansion of frequency tuning by inducing inappropriate coordinated firing of neurons across tonotopic domains through Hebbian mechanisms. Our results suggest that precise, coordinated firing of hair cells and neurons in discrete domains during early development is necessary to achieve proper tuning and frequency partitioning.

A recent study by Maul et al. (2022) used a similar approach to explore the role of spontaneous activity in auditory development by targeting TMEM16A. Genetic inactivation of *Tmem16a* resulted in a dramatic decrease in spontaneous action potential burst frequency and increased inter-spike intervals in the MNTB, similar to the firing patterns observed in SGNs from isolated *Tmem16a* KO cochleae (Wang et al., 2015), but action potential firing was not eliminated, likely because of tonic IHC depolarization. After hearing onset, these *Tmem16a* cKO mice displayed broader frequency tuning of neurons in the MNTB and impaired refinement of MNTB-LSO functional connectivity, consistent with our observations in the IC. However, MNTB neurons from *Tmem16a* cKO mice demonstrated reduced firing rates at their characteristic frequency and an ~5-dB increase in thresholds, suggestive of reduced acoustic sensitivity to low-intensity stimuli in the MNTB. We observed similar subtle trends in single-cell threshold and calcium-evoked amplitude to low-frequency, low-intensity stimuli in *Tmem16a* cKO mice (Figures S10A–S10C), but amplitudes dramatically increased at suprathreshold sound levels. Use of ketamine/xylazine anesthesia by Maul et al. (2022), which has been shown to alter spike rate, timing, and threshold in auditory neurons (Jing et al., 2021) and disrupt neuromodulatory transmission, may account for this difference. The authors relied on *Pax2-Cre* to remove *Tmem16a*, a line that displays incomplete knockout in the inner ear (Wang et al., 2015; Eckrich et al., 2019) and extensive recombination in the CNS (Ohyama and Groves, 2004).

Neuronal burst firing establishes central auditory processing domains

Sensory domains in the cerebral cortex are shaped through competitive interactions, and loss of peripheral input results in atrophy of neural territories devoted to processing that input (Rauschecker et al., 1992; Kahn and Krubitzer, 2002; De Villers-Sidani et al., 2007; Moreno-Juan et al., 2017). Disruption of pre-hearing spontaneous activity led to spatial compaction of auditory domains, reducing the area in the AC devoted to processing tonal sound information. These findings indicate that distinct patterns of activity, not simply the presence of neural activity, provides important cues to define future organization and functionality. Whether these topographic changes arise from competition with other sensory modalities or simply reflect activity-dependent stabilization is not yet known. It remains to be determined whether normal acoustic input can reverse this topographic compression of auditory domains, comparable with what can be achieved in the visual system in patients with amblyopia (Clarke et al., 2003). Our results suggest that genetic variants associated with deafness that disrupt central spontaneous activity patterns (Babola et al., 2018; Shrestha et al., 2018; Sun et al., 2018; Müller et al., 2019) may induce profound changes in the functional organization of auditory centers. Understanding the distinct changes induced by these different activity patterns may reveal new ways to enhance the performance of prosthetic hearing devices for individual patients suffering from congenital hearing loss.

Limitations of the study

Functional responses in this study were recorded exclusively to tonal stimuli in young mice, which may not reflect encoding of other sound features (such as frequency modulation) or the properties of central auditory neurons in older animals. Auditory nerve function was modestly altered in *Tmem16a* cKO mice, which may have contributed to the changes observed in the response properties of central auditory neurons. Neuronal activity was monitored with the genetically encoded calcium indicator GCaMP6s, which may not detect all differences in neuronal activity patterns.

STAR★METHODS

RESOURCE AVAILABILITY

Lead contact—Requests for sharing resources, tools, code, and reagents should be directed to the corresponding author Dwight E. Bergles (dbergles@jhmi.edu).

Materials availability—This study did not generate any unique tools or reagents.

Data and code availability

- All data reported in this paper will be shared by the lead contact upon request.
- All original code used for data analysis and figure generation is deposited on Github (https://github.com/ckersbe1/Cochlea-spont-activity-development-MS) and archived at https://doi.org/10.5281/zenodo.7195670.
- Any additional information required to reanalyze the data reported in this paper is available from the lead contact upon request.

EXPERIMENTAL MODEL AND SUBJECT DETAILS

Animals—This study was performed in strict accordance with the recommendations provided in the Guide for the Care and Use of Laboratory Animals of the National Institutes of Health. All experiments and procedures were approved by the Johns Hopkins Institutional Care and Use Committee (Protocols #M018M330, M021M290). Generation and genotyping of transgenic mice (*Tmem16a* floxed mice (Schreiber et al., 2015), *Tmem16a-GFP* mice (Huang et al., 2012), *Tecta-Cre* mice (JAX Stock No. 035552) (Babola et al., 2020), *R26-lsl-eGFP* mice (MMRRC Stock No. 32037) (Sousa et al., 2009), *R26-lsl-GCaMP3* mice (Jax Stock No. 028764) (Paukert et al., 2014), and *Snap25-T2A-GCaMP6s* mice (JAX Stock No. 025111) (Madisen et al., 2015)) have been previously described. Mice were maintained on a mixed C57Bl/6NJ-FVB/NJ background. Both male and female mice were used for all experiments in equal numbers at ages P1-P21 (precise age for each experiment can be found in the figure legends). Breeding pairs were checked daily in the morning for pups, with the date of first observation of pups defined as P0. Mice were housed on a 12-hour light/dark cycle and were provided food ad libitum.

METHOD DETAILS

Electrophysiology—Apical segments of the cochlea were acutely isolated from P0-P12 mouse pups and used within 2 hours, as described previously (Babola et al., 2021). Cochlea were superfused with aCSF at physiologic temperature (32–34 C) containing (in mM): 119 or 115 NaCl, 2.5 or 6 KCl, 1.3 $MgCl_2$, 1.3 $CaCl_2$, 1 NaH_2PO_4, 26.2 $NaHCO_3$, 11 D-glucose saturated with 95% O_2/5% CO_2 at a pH of 7.4. Whole cell recordings from ISCs and IHCs were made under visual guidance using differential interference contrast (DIC) transmitted light using a 40x magnification objective. Electrodes had tip resistances between 2.5 and 4.0 MΩ (ISCs) or between 4.0 and 6.0 MΩ (IHCs) with internal solution of (in mM): 134 KCh_3SO_3, 20 HEPES, 10 EGTA, 1 $MgCl_2$, 0.2 Na-GTP, pH 7.4. Measurements of membrane resistance in ISCs were obtained immediately through repeated 10 mV voltage steps from −20 to +20 mV relative to the holding potential. Spontaneous currents were recorded from ISCs held at −90 mV (close to resting potential) for a minimum of 10 minutes. Spontaneous currents were recorded with IHCs held at −70 mV (close to resting potential) for a minimum of 10 minutes. Recordings were performed using pClamp 9 software with a Multiclamp 700A amplifier (Axon Instruments), low pass Bessel filtered at 1 kHz, and digitized at 5 kHz (Digidata 1322a, Axon Instruments). Recordings exhibiting >20% change in access resistance or with access resistance >30 MΩ at the start of recording were discarded. Errors due to voltage drop across the series resistance and liquid junctional potential were left uncompensated. Analysis of input resistance and spontaneous activity was performed offline in MATLAB (Mathworks). Spontaneous currents were detected using the ‘peakfinder’ function, with a fixed peak threshold (baseline + 3 standard deviations) and minimum peak amplitude (10 pA for ISCs, 5 pA for IHCs).

Transmitted light imaging—For time-lapse imaging of spontaneous osmotic crenations in supporting cells, acutely excised cochleae were visualized using DIC optics through a 40x water-immersion objective coupled to a 1.8x adjustable zoom lens. Images were acquired at one frame per second using a frame grabber (LG-3; Scion) and Scion Image software. Crenations were detected by generation of difference movies in MATLAB through subtraction of frames at time t_n and t_{n+5} seconds, as described previously (Babola et al., 2020).

Cochlea explant culture and calcium imaging—Cochlea segments were acutely isolated from P6-P7 mice in ice-cold, sterile filtered, HEPES buffered artificial cerebrospinal fluid (aCSF) containing (in mM): 130 NaCl, 2.5 KCl, 10 HEPES, 1 NaH_2PO_4, 1.3 $MgCl_2$, 2.5 $CaCl_2$, 11 D-glucose, as previously described (Zhang-Hooks et al., 2016; Babola et al., 2018). Explants were mounted onto Cell-Tak (Corning) treated coverslips and incubated at 37 C for 12 hours in Dulbecco’s modified Eagle’s medium (F-12/DMEM; Invitrogen) supplemented with 1% fetal bovine serum (FBS) and 10 U/mL penicillin (Sigma) prior to imaging. After overnight culture, cochleae were transferred to the recording chamber and superfused with aCSF at physiologic temperature (32–34 C) containing (in mM): 115 NaCl, 6 KCl, 1.3 $MgCl_2$, 1.3 $CaCl_2$, 1 NaH_2PO_4, 26.2 $NaHCO_3$, 11 D-glucose saturated with 95% O_2/5% CO_2 at a pH of 7.4. Cochleae were illuminated with a 488 nm laser (maximum 25 mW power), and optical sections containing both IHCs and ISCs were obtained with a pinhole set to 3.67 Airy units, corresponding to 5.4 μm of z-depth. Images were captured at 2 Hz using a using a Zeiss laser scanning confocal microscope (LSM 710) through a 20X objective (Plan APOCHROMAT 20x/1.0 NA) at 512 × 512 pixels (425.1 by 425.1 microns) for a minimum of 10 minutes. Analysis of supporting cell and hair cell calcium transients were performed as previously described (Babola et al., 2021). Briefly, images were normalized to $\Delta F/F_o$ values at the 10th percentile, and a grid of 10 × 10 pixel squares were overlaid on the ISC region, while individual circular ROIs were placed at the basal pole of IHCs.

***In vivo* imaging of spontaneous activity—**Installation of neonatal cranial windows has been previously described (Babola et al., 2018). Briefly, mice were anesthetized in inhaled isoflurane (4% induction, 1.5% maintenance), the dorsal skull exposed and a cranial window placed over the resected intraparietal bone overlying the midbrain. After >1 hour of post-surgical recovery from anesthesia, neonatal mice were moved into a 15 mL conical tube and head-fixed under the imaging microscope. During imaging, pups were maintained at 37 C using a heating pad and temperature controller (TC-1000; CWE). Wide field epifluorescence images were captured at 10 Hz using a Hamamatsu ORCA-Flash4.0 LT digital CMOS camera attached to a Zeiss Axio Zoom.V16 stereo zoom microscope at 17x magnification illuminated continuously with a metal halide lamp (Zeiss Illuminator HXP 200C). Each recording of spontaneous activity consisted of uninterrupted acquisition over a minimum of 10 minutes. Two photon imaging was performed using a Zeiss 710 LSM microscope with two-photon excitation achieved by a Ti:sapphire laser (Chameleon Ultra II; Coherent) tuned to 920 nm. Images were collected at 4 Hz (256 × 256 pixels, 425 × 425 μm) from 150 μm Z-depth in the central IC for a minimum of 10 minutes.

Widefield imaging analysis followed previously described methods in MATLAB (Babola et al., 2018). Image intensities were normalized as $\Delta F/F_o$ values, where $\Delta F = F - F_o$ and F_o was defined as the 10th percentile value for each pixel. Oval regions of interest were placed over the right and left IC, and signal peaks were identified using built-in peak detection (‘findpeaks’) with a fixed threshold (2% $\Delta F/F_o$) and minimum peak amplitude (1% $\Delta F/F_o$). For analysis of spatial band width, a 25 × 100 rectangular ROI rotated 45–55 degrees was placed over each inferior colliculus aligned with the tonotopic axis of the IC (Babola et al., 2018). The rectangle was averaged along the short axis, creating a 100 × 1 line scan of the tonotopic axis of the IC for the duration of the time series. Events were detected using the function ‘imregionmax’ with a fixed threshold (2% $\Delta F/F_o$). Line scans of individual events were normalized to the maximum $\Delta F/F_o$ at that time point, and the band width calculated as the length along the tonotopic axis above the 75th percentile of the peak $\Delta F/F_o$. Two photon imaging analysis was performed as previously described (Kellner et al., 2021). Briefly, an array of 10 × 10 pixel grid ROIs was placed over the normalized $\Delta F/F_o$ image, and individual ROIs were considered responsive when the signal exceeded the median + 2 standard deviations. Coordinated events were defined as simultaneous activation of >2 adjoining ROIs for >1.5 s.

Analysis of neuronal activity in the superior colliculus—For assessment of spontaneous neuronal activity in the superior colliculus driven by retinal ganglion cell burst firing (Ackman et al., 2012), images were normalized to $\Delta F/F_o$ values at the 10th percentile, as described above. 200 × 150 pixel ROIs were placed over each colliculi. Pixels within each ROI were downsampled by a factor of 5 and considered active if they exceeded the mean + 3 standard deviations for that pixel. Retinal waves were defined as periods >1 s where >5 pixels were simultaneously active. Wave duration was defined as the total time in which >5 pixels were continuously active during a given retinal wave.

Cochlea and brain immunohistochemistry—Mice were deeply anesthetized with intraperitoneal injection of 10 mg/mL sodium pentobarbital (>P14) or isoflurane overdose (<P10) and cardiac perfused with ice cold 1X PBS followed by 4% paraformaldehyde (PFA) in 0.1 M phosphate buffer, pH 7.4. The brain and inner ears were carefully removed from the skull, post-fixed in 4% PFA overnight at 4 C, and stored in 1X PBS with 0.1% sodium azide. For cross sections, cochleae were decalcified in 10% EDTA in 0.1 M phosphate buffer (pH 7.4) at 4 C (P7: 2–4 hours, >P14: 48 hours), cryopreserved in 30% sucrose, embedded in O.C.T. compound (Tissue Tek), cut in 10 μm sections using a cryostat, and placed directly on slides (SuperFrost Plus, Fisher). For immunostaining, cochlea sections and free-floating whole mount cochlea were preincubated in blocking solution (0.3–0.5% Triton X-100, 5% Normal Donkey Serum in PBS, pH 7.4) and incubated overnight at 4 C (cochlea) or room temperature (brain) with primary antibodies (Chicken anti-GFP, 1:4,000, Aves; Rabbit anti-MyosinVIIA, 1:300, Proteus Biosciences; Rabbit anti-β3-tubulin, 1:500, Cell Signaling Technologies). Following overnight incubation, tissues were washed 3 × 10 minutes in PBS and incubated with corresponding donkey secondary antibodies (Alexa Fluor 488, Alexa Fluor 546, or Alexa Fluor 647; 1:2000, Invitrogen) for 2–3 hours at room temperature. Finally, tissue was washed 3 × 10 minutes in PBS, incubated with 1:10,000 DAPI in PBS, and sealed using Aqua Polymount (Polysciences, Inc). For hematoxylin and eosin staining, cochleae were decalcified and dehydrated in 70% ethanol, embedded in paraffin, cut in 5 μm sections, and stained by the Reference Histology core in the Department of Pathology at Johns Hopkins Hospital. Images were captured using an epifluorescence and light microscope (Keyence BZ-X) or a laser scanning confocal microscope (LSM 880, Zeiss). For analysis of hair cell density, decalcified cochleae were dissected and cut into 3 segments of equal length (apex, middle, base), and stained for hair cell markers as described above. Images were collected at 25x magnification at the mid-portions of each segment corresponding roughly to 8 kHz, 24 kHz, and 50 kHz, respectively. For analysis of SGNs, 10 μm-thick mid-modiolar cross-sections were identified, and images collected from the apical, middle, and basal spiral ganglia visible within that section. SGN density was determined in a blinded manner by measuring spiral ganglion area in ImageJ and subsequent manual counts of all visible Tuj1-labeled neuronal soma. If mid-modiolar sections were visualized across multiple sections and slides, images were collected from all regions and averaged.

Auditory brainstem response measurements—For assessments of auditory brainstem responses (ABRs), mice were anesthetized by intraperitoneal injection of Ketamine (100 mg/kg) and Xylazine (20 mg/kg) and placed in a sound attenuation chamber. Body temperature was maintained at 37 C using an isothermal heating pad. Subdermal platinum needle electrodes (E2, Grass Technologies) were placed posterior to the pinna, at the vertex, and leg (ground). Acoustic stimuli consisted of 0.1 ms clicks and 5 ms tone pips (2 ms rise time) of varying frequency (8, 16, 24, and 32 kHz) presented at a rate of 40 Hz. Stimuli were generated by a RZ6 processer (Tucker Davis Technologies) at sound pressure levels of 90–20 dB in 5 dB descending increments and delivered through a free-field speaker (MF-1, Tucker Davis Technologies) placed 10 cm away from the pinna. Calibration of the free-field speaker was performed using an ACO Pacific microphone (7017) and preamplifier (4016). ABR signals were amplified (Medusa 4Z, Tucker Davis Technologies), band-pass filtered (300 Hz and 3 kHz), digitized (RZ6 Processor, Tucker Davis Technologies), and averaged across 600–700 stimuli. ABR thresholds were calculated in an automated manner offline in MATLAB as the lowest stimulus intensity determined by linear interpolation that produced peak-to-peak ABR signals that were greater than 2 standard deviations above the peak-to-peak background signal. P1-N1 amplitudes and peak timing were determined using the ‘findpeaks’ function with fixed criteria. Displayed ABR traces represent mean +/− standard deviation (shaded region) across all animals.

Sound-evoked calcium imaging—Cranial windows over inferior colliculus in P13-P15 mice were performed as previously described for P7 animals, with animals allowed to recover a minimum of 2 hours prior to imaging. To enable image registration for two-photon imaging, aCSF containing Sulfarhodamine 101 (SR101, 10 μM) was washed over the brain surface before sealing of the cranial window to label astrocytes (Nimmerjahn and Helmchen, 2012). Auditory cortex (AC) windows were installed using a microblade and microscissors to remove a ~4 mm circular region of skull overlying the right auditory cortex. Following skull removal, the dura was carefully removed using microscissors and exposed brain was continuously immersed in aCSF until a 5 mm coverslip was attached using superglue. During imaging, awake animals were head-fixed but on a freely rotating tennis ball to simulate natural movement. Wide field epifluorescence images were captured as described above, with 21x magnification for AC imaging. Two photon images were captured as described above, with some modifications. Low magnification mapping was performed in the central nucleus of the IC over a 425 × 425 μm field of view at 150–200 μm Z-depth at 2 Hz (512 × 512 pixels). Following coarse mapping of pure tone responses in the IC, high magnification images were obtained along the tonotopic axis (centered on the 6 kHz response location) to assess of single cell tuning and gain through a 212 × 212 μm field of view continuously visualized at 5 Hz (256 × 256 pixels).

Acoustic stimuli were generated within the RPvdsEx software (Tucker Davis Technologies), triggered using the microscope’s frame out (widefield) or line out (two-photon) signal, and delivered through the RZ6 Processor (Tucker-Davis Technologies). Stimuli were presented using a free-field speaker (MF-1, Tucker Davis Technologies) placed 10 cm from the left ear within a custom sound attenuation chamber with external noise attenuation of 40 dB (Babola et al., 2018). Calibration of the free-field speaker was performed using an ACO Pacific microphone (7017) and preamplifier (4016). Given the flat intensity profile (peak 100 dB SPL +/− 5 dB for a 2.0 V stimulus across all tested frequencies), levels were not corrected across presented frequencies. For widefield imaging, stimuli consisted of 4 repetitions of sinusoidal amplitude modulated (SAM) pure tones (1 s, 10 Hz modulation) from 3 to 48 kHz in ¼ octave intervals. All stimuli were cosine-squared gated (5 ms) and played in a random order at 5 s intervals. Stimuli were presented from 100 dB to 40 dB SPL in 10–20 dB attenuation steps. For two-photon low magnification imaging, acoustic stimuli consisted of 1 s SAM tones from 3 to 24 kHz at 90 dB SPL. For two photon high magnification imaging, acoustic stimuli consisted of 200 ms SAM tones presented in a random order ranging from 3 to 24 kHz with 0.5 to 0.25 octave steps at 90–30 dB SPL (5–10 dB attenuation steps) with 5 s inter-stimulus intervals.

For analysis of widefield sound-evoked responses, raw images underwent bleach correction and normalization as described above for widefield imaging of spontaneous activity. Image segments were separated by tone frequency, aligned from 1 second prior to and 3 seconds following tone presentation, and averaged across the 4 presentations of each tone. Normalized and averaged images were used for display purposes. For analysis of evoked amplitude and auditory thresholds in inferior colliculus, an oval ROI was placed over the contralateral IC. For assessment of spatial band width and frequency mapping, a maximum-intensity projection of the mean sound-evoked response for each presented frequency was rotated by 45–55 degrees and a 25 × 250 pixel rectangle was placed along the tonotopic axis, centered at the 3 kHz response location for each animal. To generate the sound-evoked spatial profile, $\Delta F/F_o$ signal intensity was averaged along the short rectangle axis. Profiles were normalized to the maximum $\Delta F/F_o$ intensity (peak response location) along the tonotopic axis. The normalized spatial band width of the evoked response was defined as the width of the 75th percentile of the normalized response for each mouse. For analysis of auditory cortex response amplitudes and time course, a circular ROI was placed over A1 after visualization of averaged pure tone responses based on previously described mesoscopic maps of auditory cortex in adult mice (Issa et al., 2014; Romero et al., 2020). The low and high frequency borders of A1 were defined by their caudal and dorsal locations in auditory cortex. Thresholding and segmentation of AC pure tone foci was performed by binarizing maximum evoked responses using a fixed threshold. Images were aligned based on the 3 kHz A1 location and rotated by the angle of a vector between the 3 kHz and 48 kHz A1 foci to allow for direct comparison of tonotopic organization between animals. At P13, this process was the same except 6 and 24 kHz stimuli at 80 dB SPL were used (due to inter-animal variability in responses to the frequency extremes (3 and 48 kHz) at P13). A1 area was calculated as the total area bounded by a binarized maximum projection of activated area through a 3–48 kHz frequency sweep at 80 dB SPL (‘bw’, ‘noholes’). Cumulative auditory cortex area was calculated as the boundary encompassing the maximum aligned projection of all 3–48 kHz tone responses in all mice. Centroid separation was measured as the Euclidean distance between centroids of binarized low and high frequency foci. If motion correction was required of widefield movies, it was performed using the MOCO fast motion correction plugin (ImageJ) (Dubbs et al., 2016).

For analysis of single cell responses, images first underwent motion correction using the ImageJ plugin MultiStackReg, using SR101 signal as a fixed landmark. Next, images were aligned by tone presentation and sound level and averaged across 4–6 repetitions. ROIs were manually placed around individual sound-responsive soma and averaged, and $\Delta F/F_o$ calculated for each frequency and stimulus level, where $\Delta F = F - F_o$ and F_o represents the 20th percentile value for the ROI in the 1 s prior to tone onset across all stimuli. ROIs were considered responsive to a given stimulus if $\Delta F/F_o$ in the 1 s following stimulus onset exceeded 5 x standard deviation of the $\Delta F/F_o$ signal 1 s before stimulus onset. Maximum bandwidth was calculated as the maximum range of frequency responses within a single stimulus intensity level, while gaussian bandwidth was calculated by fitting a single term gaussian (‘fit’, ‘gauss1’) to the maximum evoked amplitude across all frequency stimuli within a given stimulus level. Frequency response area (FRA) was calculated as the integral of the total positive responses to all frequencies and sound levels with constant stimulus parameters (3–24 kHz, 40–90 dB SPL). Best frequency for a cell was defined as the stimulus frequency that elicited the maximum $\Delta F/F_o$ response at any sound level. Center frequency for a cell was defined as the stimulus frequency that elicited the maximum $\Delta F/F_o$ response at the lowest sound level that elicited a response. Neuropil analysis was performed by averaging across the entire field following application of a mask over all neuronal soma within the field identified within a maximum projection image.

QUANTIFICATION AND STATISTICAL ANALYSIS

All statistical testing was performed in MATLAB, with the results of each statistical test available in MATLAB live scripts for each figure, available at: https://github.com/ckersbe1/Cochlea-spont-activity-development-MS. All data is presented as mean +/− standard deviation, unless otherwise noted. For two-group comparisons, datasets were tested for normality using the Lilliefors test (‘lillietest’). If unable to reject the null hypothesis that the dataset is normally distributed using the Lilliefors test, an unpaired (‘ttest2’) two-tailed t-test was used to compare groups, with the addition of assumption of unequal variances (‘Vartype’, ‘unqual’) as necessary. If the null hypothesis of normality was rejected, a nonparametric Wilcoxon rank sum (‘ranksum’) test was used for unpaired samples. If multiple comparisons on the same datasets were made, a Benjamini-Hochberg correction of the false discovery rate (‘fdr_BH’) was made to adjust p values to lower the probability of type 1 errors. Comparison of cumulative distributions was performed using a two-sample Kolmogorov-Smirnov test (‘kstest2’). For datasets with multiple comparisons of non-independent samples or with missing data (ie, no stimuli at a given frequency or sound level, or data removed due to movement artifacts), a repeated measures ANOVA (‘ranova’) or a linear mixed-effects model (‘fitlme’) was used, using the reduced maximum likelihood fit method (‘FitMethod’,’reml’) and the Satterthwaite approximation of degrees of freedom. Use of a linear mixed model enabled accounting for data dependency for repeated measurements from the same mouse as a random effect. Sidák post hoc test was used to assess for post hoc comparisons as indicated in figure legends. Adjusted p-values are displayed as follows: * = $p < 0.05$, ** = $p < 0.01$, *** = $p < 0.001$, **** = $p < 0.0001$, ns = not significant. Details about number of data points and individual statistical tests and p values can be found in the figure legends.

Supplementary Material

Refer to Web version on PubMed Central for supplementary material.

ACKNOWLEDGMENTS

We thank members of the Bergles laboratory for discussions and comments on the manuscript. We thank Michele Pucak and Abigail Bush in the Multiphoton Imaging Core and Terry Shelley in the Neuroscience Machine Shop for assistance. Funding was provided by grants from the National Institutes of Health (DC008060 and NS050274 to D.E.B.). C.J.K. is supported by an individual NIH National Research Service Award (NRSA) fellowship (DC018711) and a Medical Scientist Training Program training grant (GM136577) from the National Institutes of Health.

REFERENCES

Ackman JB, Burbridge TJ, and Crair MC (2012). Retinal waves coordinate patterned activity throughout the developing visual system. Nature 490, 219–225. 10.1038/nature11529. [PubMed: 23060192]

Anthwal N, and Thompson H (2016). The development of the mammalian outer and middle ear. J. Anat. 228, 217–232. 10.1111/JOA.12344. [PubMed: 26227955]

Antón-Bolaños N, Sempere-Ferràndez A, Guillamón-Vivancos T, Martini FJ, Pérez-Saiz L, Gezelius H, Filipchuk A, Valdeolmillos M, and López-Bendito G (2019). Prenatal activity from thalamic neurons governs the emergence of functional cortical maps in mice. Science 364, 987–990. 10.1126/science.aav7617. [PubMed: 31048552]

Auerbach BD, Rodrigues PV, and Salvi RJ (2014). Central gain control in tinnitus and hyperacusis. Front. Neurol. 5, 206. 10.3389/FNEUR.2014.00206. [PubMed: 25386157]

Babola TA, Li S, Gribizis A, Lee BJ, Issa JB, Wang HC, Crair MC, and Bergles DE (2018). Homeostatic control of spontaneous activity in the developing auditory system. Neuron 99, 511–524.e5. 10.1016/j.neuron.2018.07.004. [PubMed: 30077356]

Babola TA, Kersbergen CJ, Wang HC, and Bergles DE (2020). Purinergic signaling in cochlear supporting cells reduces hair cell excitability by increasing the extracellular space. Elife 9, e52160. 10.7554/eLife.52160. [PubMed: 31913121]

Babola TA, Li S, Wang Z, Kersbergen CJ, Elgoyhen AB, Coate TM, and Bergles DE (2021). Purinergic signaling controls spontaneous activity in the auditory system throughout early development. J. Neurosci. 41, 594–612. 10.1523/JNEUROSCI.2178-20.2020. [PubMed: 33303678]

Barnstedt O, Keating P, Weissenberger Y, King AJ, and Dahmen JC (2015). Functional microarchitecture of the mouse dorsal inferior colliculus revealed through in vivo two-photon calcium imaging. J. Neurosci. 35, 10927–10939. 10.1523/JNEUROSCI.0103-15.2015. [PubMed: 26245957]

Beutner D, and Moser T (2001). The presynaptic function of mouse cochlear inner hair cells during development of hearing. J. Neurosci. 21, 4593–4599. [PubMed: 11425887]

Burbridge TJ, Xu HP, Ackman JB, Ge X, Zhang Y, Ye MJ, Zhou ZJ, Xu J, Contractor A, and Crair MC (2014). Visual circuit development requires patterned activity mediated by retinal acetylcholine receptors. Neuron 84, 1049–1064. 10.1016/j.neuron.2014.10.051. [PubMed: 25466916]

Chambers AR, Resnik J, Yuan Y, Whitton JP, Edge AS, Liberman MC, and Polley DB (2016). Central gain restores auditory processing following near-complete cochlear denervation. Neuron 89, 867–879. 10.1016/j.neuron.2015.12.041. [PubMed: 26833137]

Chandrasekaran AR, Plas DT, Gonzalez E, and Crair MC (2005). Evidence for an instructive role of retinal activity in retinotopic map refinement in the superior colliculus of the mouse. J. Neurosci. 25, 6929–6938. 10.1523/JNEUROSCI.1470-05.2005. [PubMed: 16033903]

Che A, Babij R, Iannone AF, Fetcho RN, Ferrer M, Liston C, Fishell G, and De Marco García NV (2018). Layer I interneurons sharpen sensory maps during neonatal development. Neuron 99, 98–116.e7. 10.1016/j.neuron.2018.06.002. [PubMed: 29937280]

Clarke MP, Wright CM, Hrisos S, Anderson JD, Henderson J, and Richardson SR (2003). Randomised controlled trial of treatment of unilateral visual impairment detected at preschool vision screening. BMJ 327, 1251. 10.1136/BMJ.327.7426.1251. [PubMed: 14644966]

Clause A, Kim G, Sonntag M, Weisz CJC, Vetter DE, Rűbsamen R, and Kandler K (2014). The precise temporal pattern of prehearing spontaneous activity is necessary for tonotopic map refinement. Neuron 82, 822–835. 10.1016/j.neuron.2014.04.001. [PubMed: 24853941]

Clause A, Lauer AM, and Kandler K (2017). Mice lacking the alpha9 subunit of the nicotinic acetylcholine receptor exhibit deficits in frequency difference limens and sound localization. Front. Cell. Neurosci. 11, 167. 10.3389/fncel.2017.00167. [PubMed: 28663725]

Dhande OS, Hua EW, Guh E, Yeh J, Bhatt S, Zhang Y, Ruthazer ES, Feller MB, and Crair MC (2011). Development of single retinofugal axon arbors in normal and β2 knock-out mice. J. Neurosci. 31, 3384–3399. 10.1523/JNEUROSCI.4899-10.2011. [PubMed: 21368050]

Dorrn AL, Yuan K, Barker AJ, Schreiner CE, and Froemke RC (2010). Developmental sensory experience balances cortical excitation and inhibition. Nature 465, 932–936. 10.1038/nature09119. [PubMed: 20559387]

Dubbs A, Guevara J, and Yuste R (2016). Moco: fast motion correction for calcium imaging. Front. Neuroinform. 10, 6. 10.3389/FNINF.2016.00006. [PubMed: 26909035]

Eckrich S, Hecker D, Sorg K, Blum K, Fischer K, Münkner S, Wenzel G, Schick B, and Engel J (2019). Cochlea-Specific deletion of Cav1.3 calcium channels arrests inner hair cell differentiation and unravels pitfalls of conditional mouse models. Front. Cell. Neurosci. 13, 225. 10.3389/FNCEL.2019.00225/BIBTEX. [PubMed: 31178698]

Ge X, Zhang K, Gribizis A, Hamodi AS, Sabino AM, and Crair MC (2021). Retinal waves prime visual motion detection by simulating future optic flow. Science 373, eabd0830. [PubMed: 34437090]

Geal-Dor M, Freeman S, Li G, and Sohmer H (1993). Development of hearing in neonatal rats: air and bone conducted ABR thresholds. Hear. Res. 69, 236–242. 10.1016/0378-5955(93)90113-F. [PubMed: 8226345]

Glowatzki E, and Fuchs PA (2000). Cholinergic synaptic inhibition of inner hair cells in the neonatal mammalian cochlea. Science 288, 2366–2368. 10.1126/science.288.5475.2366. [PubMed: 10875922]

Gribizis A, Ge X, Daigle TL, Ackman JB, Zeng H, Lee D, and Crair MC (2019). Visual cortex gains independence from peripheral drive before eye opening. Neuron 104, 711–723.e3. 10.1016/j.neuron.2019.08.015. [PubMed: 31561919]

Grubb MS, Rossi FM, Changeux JP, and Thompson ID (2003). Abnormal functional organization in the dorsal lateral geniculate nucleus of mice lacking the β2 subunit of the nicotinic acetylcholine receptor. Neuron 40, 1161–1172. 10.1016/S0896-6273(03)00789-X. [PubMed: 14687550]

Gu JW, Halpin CF, Nam E-C, Levine RA, and Melcher JR (2010). Tinnitus, diminished sound-level tolerance, and elevated auditory activity in humans with clinically normal hearing sensitivity. J. Neurophysiol. 104, 3361–3370. 10.1152/JN.00226.2010. [PubMed: 20881196]

Di Guilmi MN, Boero LE, Castagna VC, Rodríguez-Contreras A, Wedemeyer C, Gómez-Casati ME, and Elgoyhen AB (2019). Strengthening of the efferent olivocochlear system leads to synaptic dysfunction and tonotopy disruption of a central auditory nucleus. J. Neurosci. 39, 7037–7048. 10.1523/JNEUROSCI.2536-18.2019. [PubMed: 31217330]

Hébert S, Fournier P, and Noreña A (2013). Auditory sensitivity is increased in tinnitus ears. J. Neurosci. 33, 2356–2364. 10.1523/JNEUROSCI.3461-12.2013. [PubMed: 23392665]

Hirtz JJ, Boesen M, Braun N, Deitmer JW, Kramer F, Lohr C, Müller B, Nothwang HG, Striessnig J, Löhrke S, and Friauf E (2011). Cav1.3 calcium channels are required for normal development of the auditory brainstem. J. Neurosci. 31, 8280–8294. 10.1523/JNEUROSCI.5098-10.2011. [PubMed: 21632949]

Hirtz JJ, Braun N, Griesemer D, Hannes C, Janz K, Löhrke S, Müller B, and Friauf E (2012). Synaptic refinement of an inhibitory topographic map in the auditory brainstem requires functional Cav1.3 calcium channels. J. Neurosci. 32, 14602–14616. 10.1523/JNEUROSCI.0765-12.2012. [PubMed: 23077046]

Huang F, Zhang H, Wu M, Yang H, Kudo M, Peters CJ, Woodruff PG, Solberg OD, Donne ML, Huang X, et al. (2012). Calcium-activated chloride channel TMEM16A modulates mucin secretion and airway smooth muscle contraction. Proc. Natl. Acad. Sci. USA 109, 16354–16359. 10.1073/PNAS.1214596109/-/DCSUPPLEMENTAL. [PubMed: 22988107]

Huberman AD, Feller MB, and Chapman B (2008). Mechanisms underlying development of visual maps and receptive fields. Annu. Rev. Neurosci. 31, 479–509. 10.1146/ANNUREV.NEURO.31.060407.125533. [PubMed: 18558864]

Issa JB, Haeffele BD, Agarwal A, Bergles DE, Young ED, and Yue DT (2014). Multiscale optical Ca2+ imaging of tonal organization in mouse auditory cortex. Neuron 83, 944–959. 10.1016/j.neuron.2014.07.009. [PubMed: 25088366]

Jing Z, Pecka M, and Grothe B (2021). Ketamine-xylazine anesthesia depth affects auditory neuronal responses in the lateral superior olive complex of the gerbil. J. Neurophysiol. 126, 1660–1669. 10.1152/JN.00217.2021. [PubMed: 34644166]

Johnson SL, Eckrich T, Kuhn S, Zampini V, Franz C, Ranatunga KM, Roberts TP, Masetto S, Knipper M, Kros CJ, and Marcotti W (2011). Position-dependent patterning of spontaneous action potentials in immature cochlear inner hair cells. Nat. Neurosci. 14, 711–717. 10.1038/nn.2803. [PubMed: 21572434]

Kahn DM, and Krubitzer L (2002). Massive cross-modal cortical plasticity and the emergence of a new cortical area in developmentally blind mammals. Proc. Natl. Acad. Sci. USA 99, 11429–11434. 10.1073/pnas.162342799. [PubMed: 12163645]

Kandler K, Clause A, and Noh J (2009). Tonotopic reorganization of developing auditory brainstem circuits. Nat. Neurosci. 12, 711–717. 10.1038/nn.2332. [PubMed: 19471270]

Katz LC, and Shatz CJ (1996). Synaptic activity and the construction of cortical circuits. Science 274, 1133–1138. 10.1126/science.274.5290.1133. [PubMed: 8895456]

Kellner V, Kersbergen CJ, Li S, Babola TA, Saher G, and Bergles DE (2021). Dual metabotropic glutamate receptor signaling enables coordination of astrocyte and neuron activity in developing sensory domains. Neuron 109, 2545–2555.e7. 10.1016/j.neuron.2021.06.010. [PubMed: 34245686]

Kirkby LA, Sack GS, Firl A, and Feller MB (2013). A role for correlated spontaneous activity in the assembly of neural circuits. Neuron 80, 1129–1144. 10.1016/j.neuron.2013.10.030. [PubMed: 24314725]

Kotak VC, Fujisawa S, Lee FA, Karthikeyan O, Aoki C, and Sanes DH (2005). Hearing loss raises excitability in the auditory cortex. J. Neurosci. 25, 3908–3918. 10.1523/JNEUROSCI.5169-04.2005. [PubMed: 15829643]

Kotak VC, Takesian AE, and Sanes DH (2008). Hearing loss prevents the maturation of GABAergic transmission in the auditory cortex. Cereb. Cortex 18, 2098–2108. 10.1093/cercor/bhm233. [PubMed: 18222937]

Leake PA, Hradek GT, Chair L, and Snyder RL (2006). Neonatal deafness results in degraded topographic specificity of auditory nerve projections to the cochlear nucleus in cats. J. Comp. Neurol. 497, 13–31. 10.1002/cne.20968. [PubMed: 16680765]

Leao RN, Sun H, Svahn K, Berntson A, Youssoufian M, Paolini AG, Fyffe REW, and Walmsley B (2006). Topographic organization in the auditory brainstem of juvenile mice is disrupted in congenital deafness. J. Physiol. 571, 563–578. 10.1113/jphysiol.2005.098780. [PubMed: 16373385]

Lippe WR (1994). Rhythmic spontaneous activity in the developing avian auditory system. J. Neurosci. 14, 1486–1495. 10.1523/jneurosci.14-03-01486.1994. [PubMed: 8126550]

Madisen L, Garner AR, Shimaoka D, Chuong AS, Klapoetke NC, Li L, van der Bourg A, Niino Y, Egolf L, Monetti C, et al. (2015). Transgenic mice for intersectional targeting of neural sensors and effectors with high specificity and performance. Neuron 85, 942–958. 10.1016/j.neuron.2015.02.022. [PubMed: 25741722]

Marco EJ, Hinkley LB, Hill SS, and Nagarajan SS (2011). Sensory processing in autism: a review of neurophysiologic findings. Pediatric Res. 69, 48–54.

Martini FJ, Guillamón-Vivancos T, Moreno-Juan V, Valdeolmillos M, and López-Bendito G (2021). Spontaneous activity in developing thalamic and cortical sensory networks. Neuron 109, 2519–2534. 10.1016/J.NEURON.2021.06.026. [PubMed: 34293296]

Maul A, Huebner AK, Strenzke N, Moser T, Rübsamen R, Jovanovic S, and Hübner CA (2022). The Cl–channel TMEM16A is involved in the generation of cochlear Ca2+ waves and promotes the refinement of auditory brainstem networks in mice. Elife 11, e72251. 10.7554/ELIFE.72251. [PubMed: 35129434]

McKay SM, and Oleskevich S (2007). The role of spontaneous activity in development of the endbulb of Held synapse. Hear. Res. 230, 53–63. 10.1016/j.heares.2007.05.006. [PubMed: 17590547]

Mikaelian D, and Ruben RJ (1965). Development of hearing in the normal cba-j mouse: correlation of physiological observations with behavioral responses and with cochlear anatomy. Acta Otolaryngol. 59, 451–461. 10.3109/00016486509124579.

Mizuno H, Ikezoe K, Nakazawa S, Sato T, Kitamura K, and Iwasato T (2018). Patchwork-type spontaneous activity in neonatal barrel cortex layer 4 transmitted via thalamocortical projections. Cell Rep. 22, 123–135. 10.1016/j.celrep.2017.12.012. [PubMed: 29298415]

Moreno-Juan V, Filipchuk A, Antón-Bolaños N, Mezzera C, Gezelius H, Andrés B, Rodríguez-Malmierca L, Susín R, Schaad O, Iwasato T, et al. (2017). Prenatal thalamic waves regulate cortical area size prior to sensory processing. Nat. Commun. 8, 14172. 10.1038/ncomms14172. [PubMed: 28155854]

Mostafapour SP, Cochran SL, Del Puerto NM, and Rubel EW (2000). Patterns of cell death in mouse anteroventral cochlear nucleus neurons after unilateral cochlea removal. J. Comp. Neurol. 426, 561–571. 10.1002/1096-9861(20001030)426:4<561::AID-CNE5>3.0.CO;2-g. [PubMed: 11027399]

Mrsic-Flogel TD, Hofer SB, Creutzfeldt C, Cloëz-Tayarani I, Changeux JP, Bonhoeffer T, and Hübener M (2005). Altered map of visual space in the superior colliculus of mice lacking early retinal waves. J. Neurosci. 25, 6921–6928. 10.1523/JNEUROSCI.1555-05.2005. [PubMed: 16033902]

Müller NIC, Sonntag M, Maraslioglu A, Hirtz JJ, and Friauf E (2019). Topographic map refinement and synaptic strengthening of a sound localization circuit require spontaneous peripheral activity. J. Physiol. 597, 5469–5493. 10.1113/JP277757. [PubMed: 31529505]

Nimmerjahn A, and Helmchen F (2012). In vivo labeling of cortical astrocytes with sulforhodamine 101 (SR101). Cold Spring Harb. Protoc. 2012, 326–334. 10.1101/PDB.PROT068155. [PubMed: 22383644]

Noh J, Seal RP, Garver JA, Edwards RH, and Kandler K (2010). Glutamate co-release at GABA/glycinergic synapses is crucial for the refinement of an inhibitory map. Nat. Neurosci. 13, 232–238. 10.1038/nn.2478. [PubMed: 20081852]

Ohyama T, and Groves AK (2004). Generation of Pax2-Cre mice by modification of a Pax2 bacterial artificial chromosome. Genesis 38, 195–199. 10.1002/gene.20017. [PubMed: 15083520]

Paukert M, Agarwal A, Cha J, Doze VA, Kang JU, and Bergles DE (2014). Norepinephrine controls astroglial responsiveness to local circuit activity. Neuron 82, 1263–1270. 10.1016/j.neuron.2014.04.038. [PubMed: 24945771]

Penagarikano O, Mulle JG, and Warren ST (2007). The pathophysiology of fragile X syndrome. Annu. Rev. Genom. Human Genet. 8, 109–129. 10.1146/annurev.genom.8.080706.092249.

Rauschecker JP, Tian B, Korte M, and Egert U (1992). Crossmodal changes in the somatosensory vibrissa/barrel system of visually deprived animals. Proc. Natl. Acad. Sci. USA 89, 5063–5067. 10.1073/PNAS.89.11.5063. [PubMed: 1594614]

Romero S, Hight AE, Clayton KK, Resnik J, Williamson RS, Hancock KE, and Polley DB (2020). Cellular and widefield imaging of sound frequency organization in primary and higher order fields of the mouse auditory cortex. Cereb. Cortex 30, 1603–1622. 10.1093/cercor/bhz190. [PubMed: 31667491]

Schreiber R, Faria D, Skryabin BV, Wanitchakool P, Rock JR, and Kunzelmann K (2015). Anoctamins support calcium-dependent chloride secretion by facilitating calcium signaling in adult mouse intestine. Pflugers Arch. 467, 1203–1213. 10.1007/S00424-014-1559-2/FIGURES/7. [PubMed: 24974903]

Scott LL, Mathews PJ, and Golding NL (2005). Posthearing developmental refinement of temporal processing in principal neurons of the medial superior olive. J. Neurosci. 25, 7887–7895. 10.1523/JNEUROSCI.1016-05.2005. [PubMed: 16135745]

Shrestha BR, Chia C, Wu L, Kujawa SG, Liberman MC, and Goodrich LV (2018). Sensory neuron diversity in the inner ear is shaped by activity. Cell 174, 1229–1246.e17. 10.1016/j.cell.2018.07.007. [PubMed: 30078709]

Siegel F, Heimel JA, Peters J, and Lohmann C (2012). Peripheral and central inputs shape network dynamics in the developing visual cortex in vivo. Curr. Biol. 22, 253–258. 10.1016/J.CUB.2011.12.026. [PubMed: 22264606]

Sitko AA, and Goodrich LV (2021). Making sense of neural development by comparing wiring strategies for seeing and hearing. Science 371, eaaz6317. 10.1126/science.aaz6317. [PubMed: 33414193]

Sonntag M, Englitz B, Kopp-Scheinpflug C, and Rübsamen R (2009). Early postnatal development of spontaneous and acoustically evoked discharge activity of principal cells of the medial nucleus of the trapezoid body: an in vivo study in mice. J. Neurosci. 29, 9510–9520. 10.1523/JNEUROSCI.1377-09.2009. [PubMed: 19641114]

Sousa VH, Miyoshi G, Hjerling-Leffler J, Karayannis T, and Fishell G (2009). Characterization of Nkx6–2-derived neocortical interneuron lineages. Cereb. Cortex 19, 1–10. 10.1093/cercor/bhp038. [PubMed: 18448452]

Stiebler I, and Ehret G (1985). Inferior colliculus of the house mouse. I. A quantitative study of tonotopic organization, frequency representation, and tone-threshold distribution. J. Comp. Neurol. 238, 65–76. 10.1002/cne.902380106. [PubMed: 4044904]

Stouffer JL, and Tyler RS (1990). Characterization of tinnitus by tinnitus patients. J. Speech Hear. Disord. 55, 439–453. 10.1044/JSHD.5503.439. [PubMed: 2381186]

Sun S, Babola T, Pregernig G, So KS, Nguyen M, Su SSM, Palermo AT, Bergles DE, Burns JC, and Müller U (2018). Hair cell mechanotransduction regulates spontaneous activity and spiral ganglion subtype specification in the auditory system. Cell 174, 1247–1263.e15. 10.1016/j.cell.2018.07.008. [PubMed: 30078710]

Sun YJ, Wu GK, Liu BH, Li P, Zhou M, Xiao Z, Tao HW, and Zhang LI (2010). Fine-tuning of pre-balanced excitation and inhibition during auditory cortical development. Nature 465, 927–931. 10.1038/nature09079. [PubMed: 20559386]

Tierney TS, Russell FA, and Moore DR (1997). Susceptibility of developing cochlear nucleus neurons to deafferentation-induced death abruptly ends just before the onset of hearing. J. Comp. Neurol. 378, 295–306. 10.1002/(SICI)1096-9861(19970210)378:2<295::AIDCNE11>3.0.CO;2-r. [PubMed: 9120067]

Tiriac A, Bistrong K, Pitcher MN, Tworig JM, and Feller MB (2022). The influence of spontaneous and visual activity on the development of direction selectivity maps in mouse retina. Cell Rep. 38. 10.1016/J.CELREP.2021.110225.

Tong L, Strong MK, Kaur T, Juiz JM, Oesterle EC, Hume C, Warchol ME, Palmiter RD, and Rubel EW (2015). Selective deletion of cochlear hair cells causes rapid age-dependent changes in spiral ganglion and cochlear nucleus neurons. J. Neurosci. 35, 7878–7891. 10.1523/JNEUROSCI.2179-14.2015. [PubMed: 25995473]

Tritsch NX, Yi E, Gale JE, Glowatzki E, and Bergles DE (2007). The origin of spontaneous activity in the developing auditory system. Nature 450, 50–55. 10.1038/nature06233. [PubMed: 17972875]

Tritsch NX, Rodríguez-Contreras A, Crins TTH, Wang HC, Borst JGG, and Bergles DE (2010). Calcium action potentials in hair cells pattern auditory neuron activity before hearing onset. Nat. Neurosci. 13, 1050–1052. 10.1038/nn.2604. [PubMed: 20676105]

Tritsch NX, and Bergles DE (2010). Developmental regulation of spontaneous activity in the mammalian cochlea. J. Neurosci. 30, 1539–1550. 10.1523/JNEUROSCI.3875-09.2010. [PubMed: 20107081]

Vale C, and Sanes DH (2000). Afferent regulation of inhibitory synaptic transmission in the developing auditory midbrain. J. Neurosci. 20, 1912–1921. 10.1523/JNEUROSCI.20-05-01912.2000. [PubMed: 10684892]

Vale C, and Sanes DH (2002). The effect of bilateral deafness on excitatory and inhibitory synaptic strength in the inferior colliculus. Eur. J. Neurosci. 16, 2394–2404. 10.1046/J.1460-9568.2002.02302.X. [PubMed: 12492434]

De Villers-Sidani E, Chang EF, Bao S, and Merzenich MM (2007). Critical period window for spectral tuning defined in the primary auditory cortex (A1) in the rat. J. Neurosci. 27, 180–189. 10.1523/JNEUROSCI.3227-06.2007. [PubMed: 17202485]

Wang HC, Lin CC, Cheung R, Zhang-Hooks Y, Agarwal A, Ellis-Davies G, Rock J, and Bergles DE (2015). Spontaneous activity of cochlear hair cells triggered by fluid secretion mechanism in adjacent support cells. Cell 163, 1348–1359. 10.1016/j.cell.2015.10.070. [PubMed: 26627734]

Wang Y, Sanghvi M, Gribizis A, Zhang Y, Song L, Morley B, Barson DG, Santos-Sacchi J, Navaratnam D, and Crair M (2021). Efferent feedback controls bilateral auditory spontaneous activity. Nat. Commun. 12, 2449. 10.1038/s41467-021-22796-8. [PubMed: 33907194]

Wong AB, and Borst JGG (2019). Tonotopic and non-auditory organization of the mouse dorsal inferior colliculus revealed by two-photon imaging. Elife 8, e49091. 10.7554/eLife.49091. [PubMed: 31612853]

Wong FK, and Marín O (2019). Developmental cell death in the cerebral cortex. Annu. Rev. Cell Dev. Biol. 35, 523–542. 10.1146/ANNUREV-CELLBIO-100818-125204. [PubMed: 31283379]

Yu CR, Power J, Barnea G, O’Donnell S, Brown HEV, Osborne J, Axel R, and Gogos JA (2004). Spontaneous neural activity is required for the establishment and maintenance of the olfactory sensory map. Neuron 42, 553–566. 10.1016/S0896-6273(04)00224-7. [PubMed: 15157418]

Zhang-Hooks Y, Agarwal A, Mishina M, and Bergles DE (2016). NMDA receptors enhance spontaneous activity and promote neuronal survival in the developing cochlea. Neuron 89, 337–350. 10.1016/j.neuron.2015.12.016. [PubMed: 26774161]

Highlights

- Auditory system spontaneous activity prior to hearing onset requires cochlear TMEM16A
- Disruption of spontaneous activity leads to enhanced gain of auditory neurons
- Neurons respond to a broader sound frequency range when deprived of pre-hearing activity
- Sound-responsive brain regions are smaller in the absence of spontaneous activity

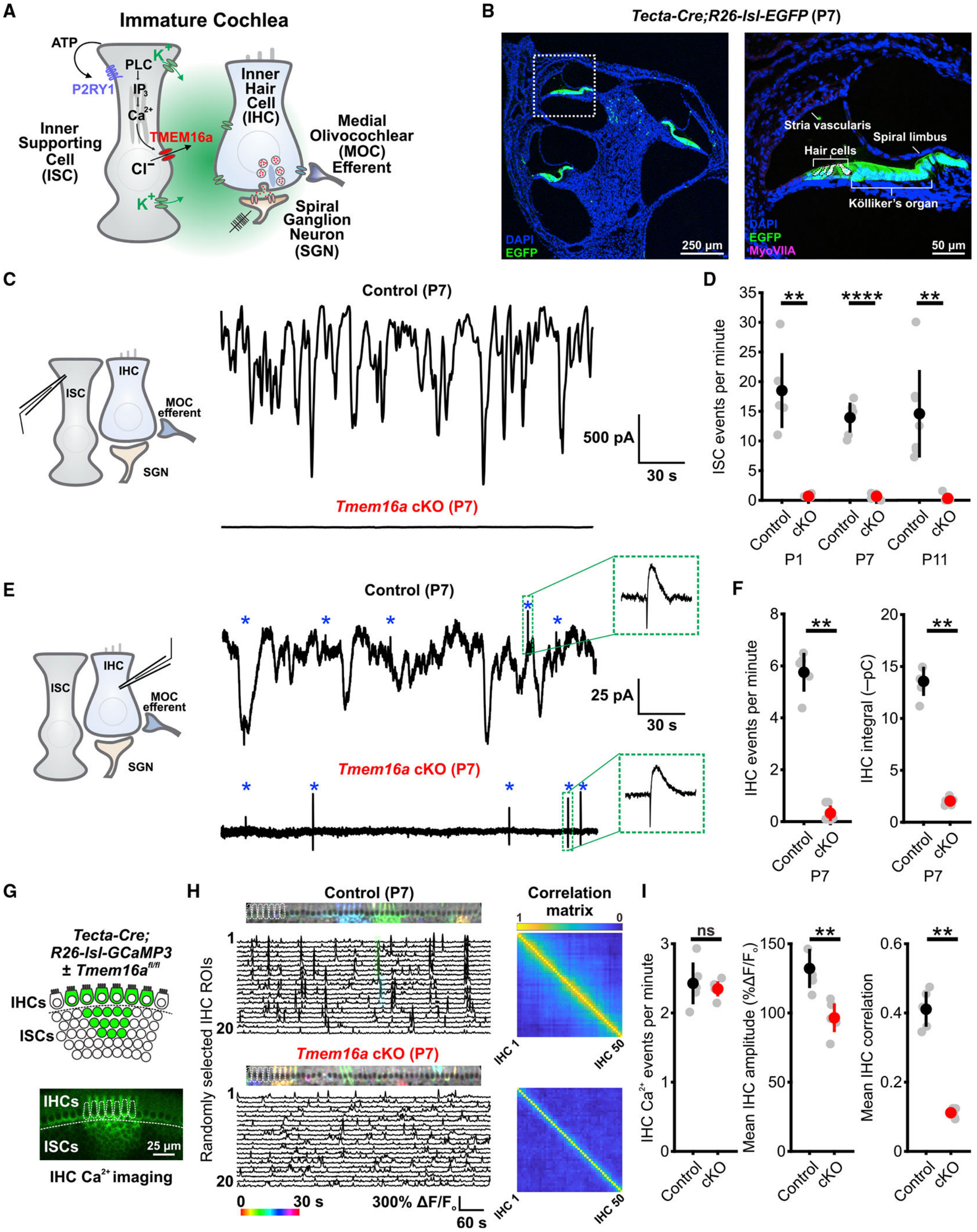

Figure 1. TMEM16A channels are required for spontaneous activity in the immature cochlea

(A) Mechanism of spontaneous auditory neural activity generation by inner supporting cells (ISCs) in the developing cochlea.

(B) Extent of recombination of *Tecta-Cre* in a cross-section of the immature post-natal day 7 (P7) cochlea, as shown by EGFP (green) reporter expression. A white square indicates the site of high magnification. IHCs and outer hair cells are labeled by immunoreactivity to Myosin VIIa (MyoVIIa; magenta, circled by black dashed lines).

(C) Whole-cell patch-clamp recordings of spontaneous activity from P7 control (*Tmem16a*$^{fl/fl}$) and P7 *Tmem16a* cKO (*Tecta-Cre;Tmem16a*$^{fl/fl}$) ISCs in acutely isolated cochleae.

(D) Quantification of spontaneous inward current frequency in ISCs at three ages (P1, P7, P11) encompassing postnatal development. Gray circles represent individual animals, colored circles represent the mean value, and error bars represent standard deviation. n = 5, 6, 7 control ISCs; n = 6, 6, 7 *Tmem16a* cKO ISCs (P1, P7, P11); p = 0.0043, 4.1330e–7, 0.0061 (P1, P7, P11), Wilcoxon rank-sum test (P1, P11) or two-sample t test (P7) with Benjamini-Hochberg correction for multiple comparisons.

(E) Whole-cell patch-clamp recordings of spontaneous activity from P7 control and P7 *Tmem16a* cKO inner hair cells (IHCs) in acutely isolated cochleae. Asterisks indicate the medial olivocochlear (MOC) efferent synaptic response (inset) present in control and *Tmem16a* cKO recordings.

(F) Quantification of spontaneous inward current frequency and integral (charge transfer) in IHCs at P7. n = 5 control IHCs, 6 *Tmem16a* cKO IHCs; p = 0.0043, 0.0043 (frequency, integral), Wilcoxon rank-sum test with Benjamini-Hochberg correction.

(G) Schematic depicting calcium imaging in IHCs in excised cochlea that express a Cre-dependent genetically encoded calcium indicator, GCaMP3. Regions of interest (ROIs) are placed over each IHC.

(H) Left: pseudocolored projection of IHC spontaneous calcium activity over 30 s and corresponding raster plot over 10 min in control (*Tecta-Cre;Tmem16a*$^{fl/+}$*; R26-lsl-GCaMP3*) and *Tmem16a* cKO (*Tecta-Cre;Tmem16a*$^{fl/fl}$*;R26-lsl-GCaMP3*) cochleae. Right: mean correlation matrix of calcium activity between individual IHCs. n = 5 control, 6 *Tmem16a* cKO cochleae.

(I) Quantification of spontaneous calcium transients in IHCs. n = 5 control, 6 *Tmem16a* cKO cochleae; p = 0.7922, 0.0065, 0.0065 (frequency, amplitude, correlation), Wilcoxon rank-sum test with Benjamini-Hochberg correction.

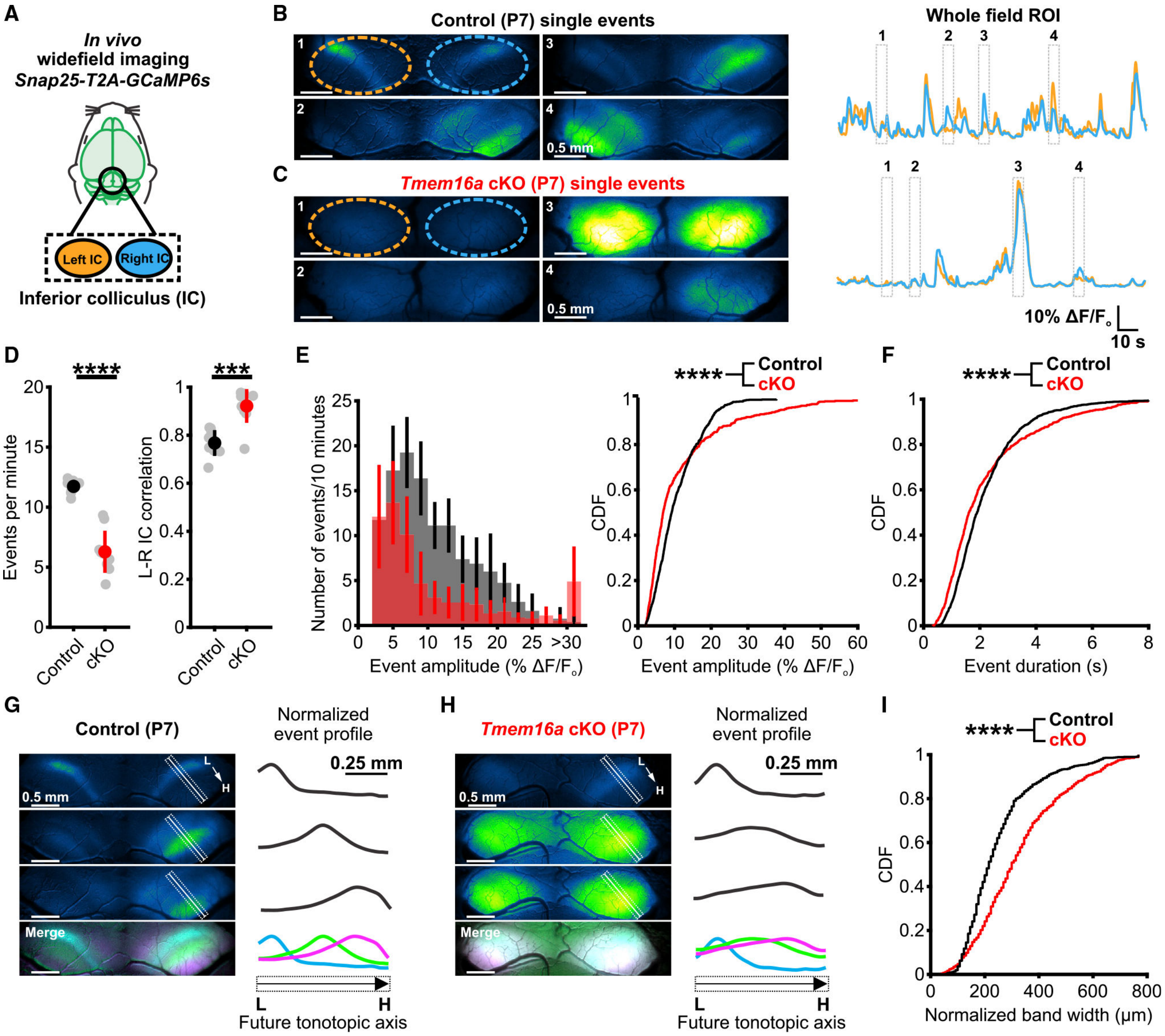

Figure 2. Deletion of *Tmem16a* suppresses calcium transients in central auditory neurons prior to hearing onset

(A) *In vivo* wide-field imaging paradigm to visualize spontaneous neural activity in the inferior colliculus (IC) of unanesthetized mouse pups.

(B) Left: four example calcium transients from P7 control (*Tmem16a*$^{fl/fl}$*;Snap25-T2A-GCaMP6s*) mice. Colored dashed circles denote left and right ROIs. Right: fluorescence trace over time of spontaneous activity in the left (orange) and right (blue) IC with example single events highlighted.

(C) Same as (B) but from P7 *Tmem16a* cKO (*Tecta-Cre;Tmem16a*$^{fl/fl}$*;Snap25-T2A-GCaMP6s*) mice.

(D) Quantification of spontaneous event frequency and left-right IC correlation. n = 8 control mice, 9 *Tmem16a* cKO mice; p = 1.0033e–5, 2.6549e–4 (frequency, correlation), two-sample t test with unequal variances (frequency) or Wilcoxon rank-sum test (correlation) and Benjamini-Hochberg correction.

(E) Left: histogram of spontaneous event amplitude. Right: cumulative distribution of spontaneous event amplitude. n = 940 events from 8 control mice, 560 events from 9 *Tmem16a* cKO mice; p = 6.4020e–11, two-sample Kolmogorov-Smirnov test with Benjamini-Hochberg correction.

(F) Cumulative distribution of spontaneous event duration. n = 940 events from 8 control mice, 560 events from 9 *Tmem16a* cKO mice; p = 6.373e–6, two-sample Kolmogorov-Smirnov test with Benjamini-Hochberg correction.

(G) Left: calcium transients in control mice within restricted bands along the future tonotopic axis (low [L] to high ;H] frequency) of the IC in P7 control mice. A white box indicates averaged the region (along the short axis) to generate the spatial tonotopic fluorescence profile. The pseudocolored merged image highlights distinct activation domains by each event. Right: plot of the spatial fluorescence profile along the future tonotopic axis, normalized to peak fluorescence change, for the spontaneous event to the left.

(H) Same as (G) but from a P7 *Tmem16a* cKO mouse.

(I) Cumulative distribution of normalized bandwidth (75th percentile) for spontaneous events. n = 986 events from 6 control mice, 550 events from 8 *Tmem16a* cKO mice; p = 1.6325e–23, two-sample Kolmogorov-Smirnov test.

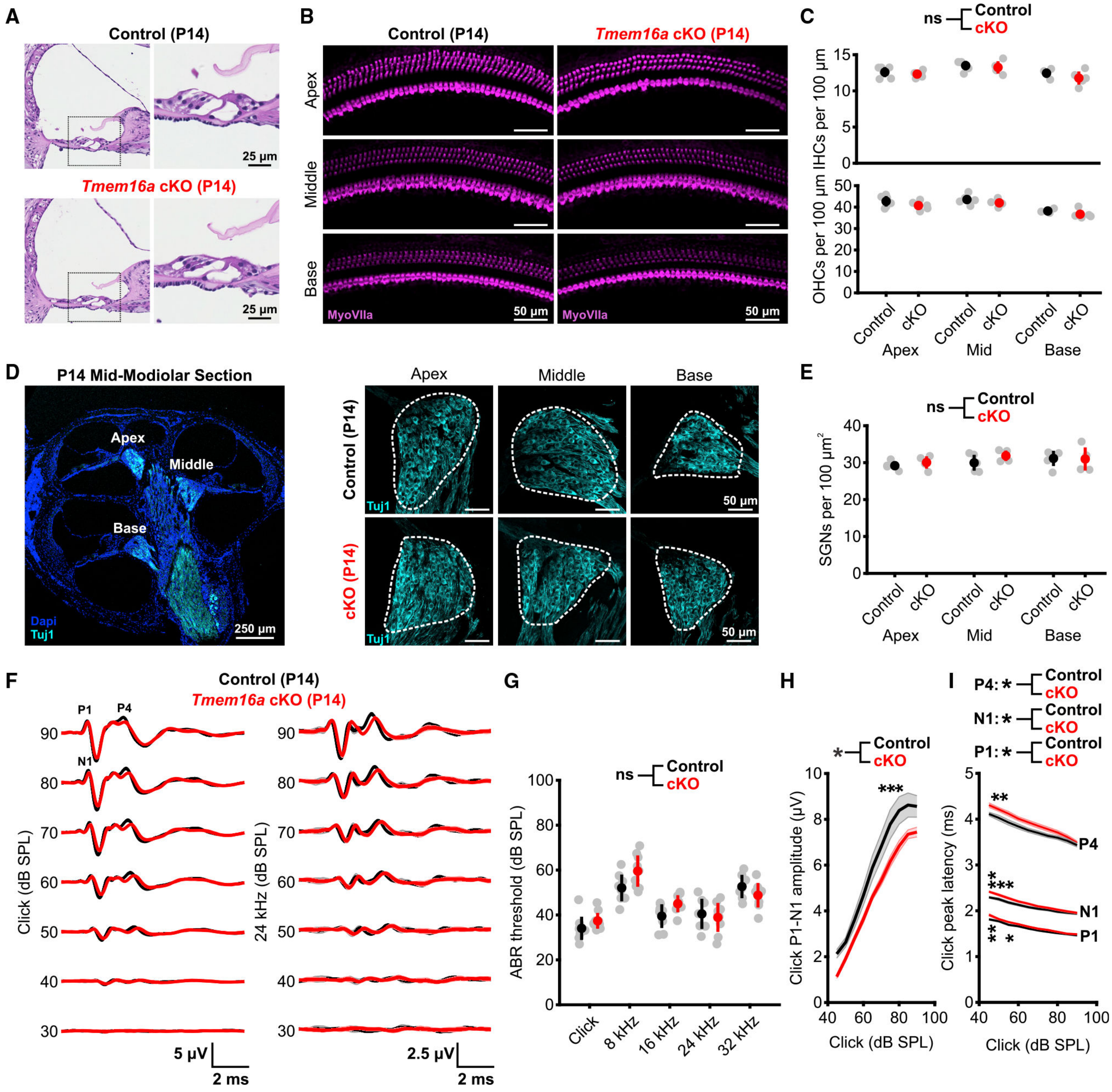

Figure 3. Cochlear structure and sound detection are preserved in *Tmem16a* cKO mice

(A) Hematoxylin and eosin staining of cross-sections from P14 control (*Tmem16a*$^{fl/fl}$) and *Tmem16a* cKO (*Tecta-Cre;Tmem16a*$^{fl/fl}$) basal cochleae. A black square indicates the region of high magnification.

(B) Hair cells in whole-mount preparations of apical, middle, and basal P14 control and *Tmem16a* cKO cochleae labeled by immunoreactivity to MyoVIIa (magenta).

(C) Quantification of IHC and outer hair cell (OHC) density. n = 6 cochleae from 6 control mice, 5 cochleae from 5 *Tmem16a* cKO mice; p = 0.2392, 0.0840 (IHCs, OHCs), linear mixed model.

(D) Left: low-magnification, mid-modiolar cross-section of a P14 cochlea with spiral ganglion neurons (SGNs) labeled by immunoreactivity to β-III tubulin (Tuj1, cyan). Right: high-magnification images of SGN somata in apical, middle, and basal regions of the cochlea in P14 control and *Tmem16a* cKO mice.

(E) Quantification of SGN density. n = 5 cochleae from 5 control mice, 4 cochleae from 4 *Tmem16a* cKO mice; p = 0.5057, linear mixed model.

(F) Mean auditory brain stem response (ABR) trace to click (left) or 24-kHz pure-tone pip (right) stimuli from 90- to 20-dB sound pressure level (SPL) in P14 control and *Tmem16a* cKO mice. P1, ABR peak 1; N1, ABR trough 1; P4, ABR peak 4.

(G) Quantification of ABR threshold to click and pure-tone stimuli. n = 9 control mice, 10 *Tmem16a* cKO mice; p = 0.0962, linear mixed model.

(H) Quantification of click ABR wave 1 (P1:N1) amplitude across a range of sound levels. n = 9 control mice, 10 *Tmem16a* cKO mice; mean ± SEM, p = 0.0143, linear mixed model with Sidák post hoc test.

(I) Quantification of click ABR wave latency (P1, N1, P4) across a range of sound levels. n = 9 control mice, 10 *Tmem16a* cKO mice; mean ± SEM, *p = 0.0203, 0.0358, 0.0305 (P1, N1, P4), linear mixed model with Sidák post hoc test.

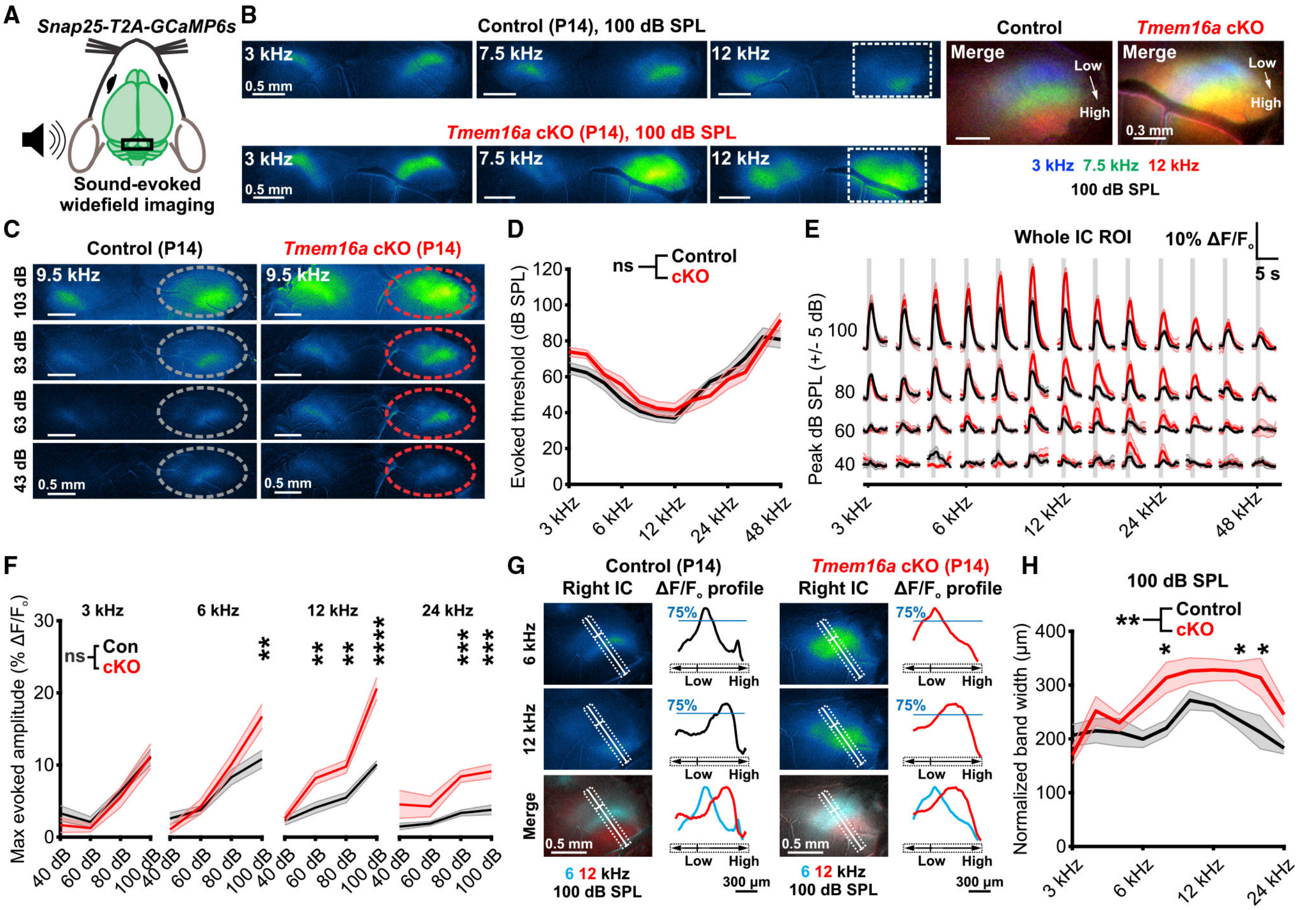

Figure 4. Disruption of pre-hearing spontaneous activity enhances the gain of central auditory neurons

(A) *In vivo* wide-field imaging of tone-evoked IC neural activity in unanesthetized mice after hearing onset.

(B) Tone-evoked neural calcium transients in the IC from P14 control (*Tmem16a*$^{fl/fl}$;*Snap25-T2A-GCaMP6s*) and P14 *Tmem16a* cKO (*Tecta-Cre;Tmem16a*$^{fl/fl}$;*Snap25-T2A-GCaMP6s*) mice at 100-dB SPL. A merged and magnified image of the right IC (right) shows tonotopic segregation of pseudocolored pure tone responses; cyan and yellow colors indicate areas of overlap.

(C) IC neural calcium transients to a 9.5-kHz stimulus from 103- to 43-dB SPL)in a control and *Tmem16a* cKO mouse. A circle in the right IC depicts the ROI for subsequent quantification of threshold and amplitude.

(D) Quantification of pure tone sound-evoked thresholds. n = 11 control mice, 8 *Tmem16a* cKO mice; p = 0.0941, repeated measures ANOVA with lower bound p value adjustment.

(E) Quantification of tone-evoked fluorescence in the IC across a range of frequency and sound level stimuli in control and *Tmem16a* cKO mice. A vertical gray bar indicates tone presentation. n = 9–12 control mice, 5–10 *Tmem16a* cKO mice, mean ± SEM.

(F) Rate-level functions characterizing maximum whole IC response amplitude at 3, 6, 12, and 24 kHz. n = 9–12 control mice, 5–10 *Tmem16a* cKO mice; linear mixed model with Sidák post hoc test.

(G) Measurement of pure-tone-evoked spatial activation (75th percentile) normalized to peak fluorescence response amplitude along the tonotopic axis of the IC at 100-dB SPL.

(H) Quantification of spatial evoked fluorescence along the tonotopic axis at 100-dB SPL. n = 9 control mice, 8 *Tmem16a* cKO mice; mean ± SEM, p = 0.0057, linear mixed model with Sidák post hoc test.

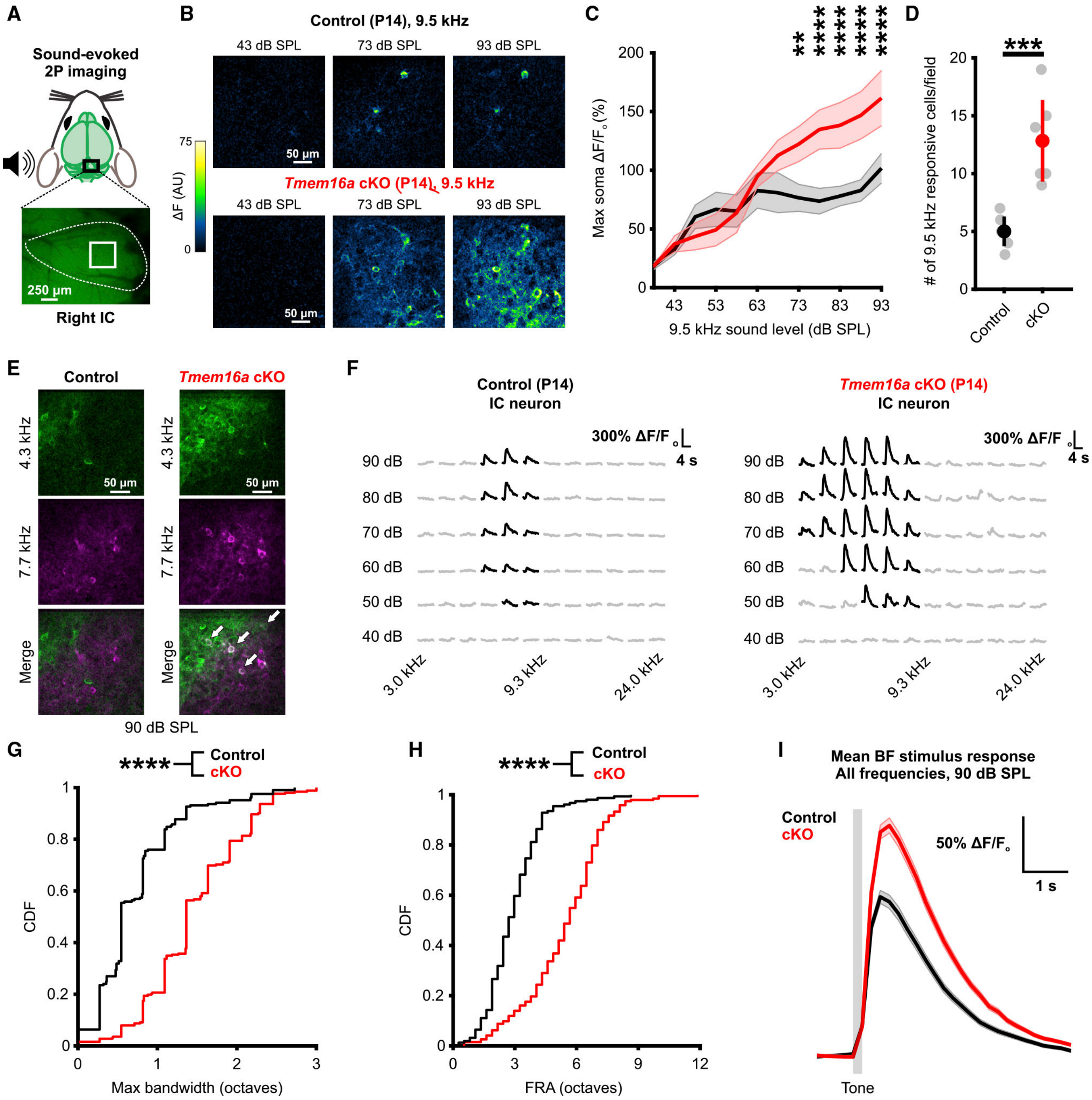

Figure 5. Disrupted patterns of pre-hearing spontaneous activity elicit broadening of receptive fields

(A) Schematic depicting the site of two-photon (2P) imaging in the central nucleus of the IC in P14 mice.

(B) 2P high-magnification imaging of tone-evoked fluorescence to increasing sound levels in IC neurons and neuropil in P14 control (*Tmem16a*$^{fl/fl}$*;Snap25-T2A-GCaMP6s*) and *Tmem16a* cKO (*Tecta-Cre;Tmem16a*$^{fl/fl}$*;Snap25-T2A-GCaMP6s*) mice.

(C) Fluorescence changes in responsive neuronal somata elicited by increasing intensity of a 9.5-kHz pure tone. n = 6 control mice (30 cells), 6 *Tmem16a* cKO mice (77 cells); mean ± SEM, p = 0.0417, linear mixed model with Sidák post hoc test.

(D) Quantification of the number of responsive neurons to a 9.5-kHz pure tone in the fixed imaging field. n = 6 control mice, 6 *Tmem16a* cKO mice; p = 8.9678e–4, two-sample t test with unequal variances.

(E) Pseudocolored tone-evoked fluorescence in IC neurons at 90-dB SPL in a control and *Tmem16a* cKO mouse. White arrows indicate neurons responsive to both stimuli in the merged image.

(F) Fluorescence changes in a representative IC neuron to a range of frequency and intensity stimuli in a control and *Tmem16a* cKO mouse. Black traces represent positive responses to the stimulus, and gray traces indicate unresponsiveness to the stimulus.

(G) Quantification of maximum frequency bandwidth of IC neurons at any sound level. n = 207 control cells (8 mice), 252 *Tmem16a* cKO cells (7 mice); p = 4.7586e–32, two-sample Kolmogorov-Smirnov test.

(H) Cumulative distribution of frequency response area (FRA) of tone-responsive neural somata in the IC. n = 157 control cells (6 mice), 193 *Tmem16a* cKO cells (4 mice); p = 1.2817e–31, two-sample Kolmogorov-Smirnov test.

(I) Mean fluorescence change in response to a neuron’s best frequency stimulus at 90-dB SPL. A vertical bar indicates tone presentation. n = 235 control cells, 295 *Tmem16a* cKO cells; mean ± SEM.

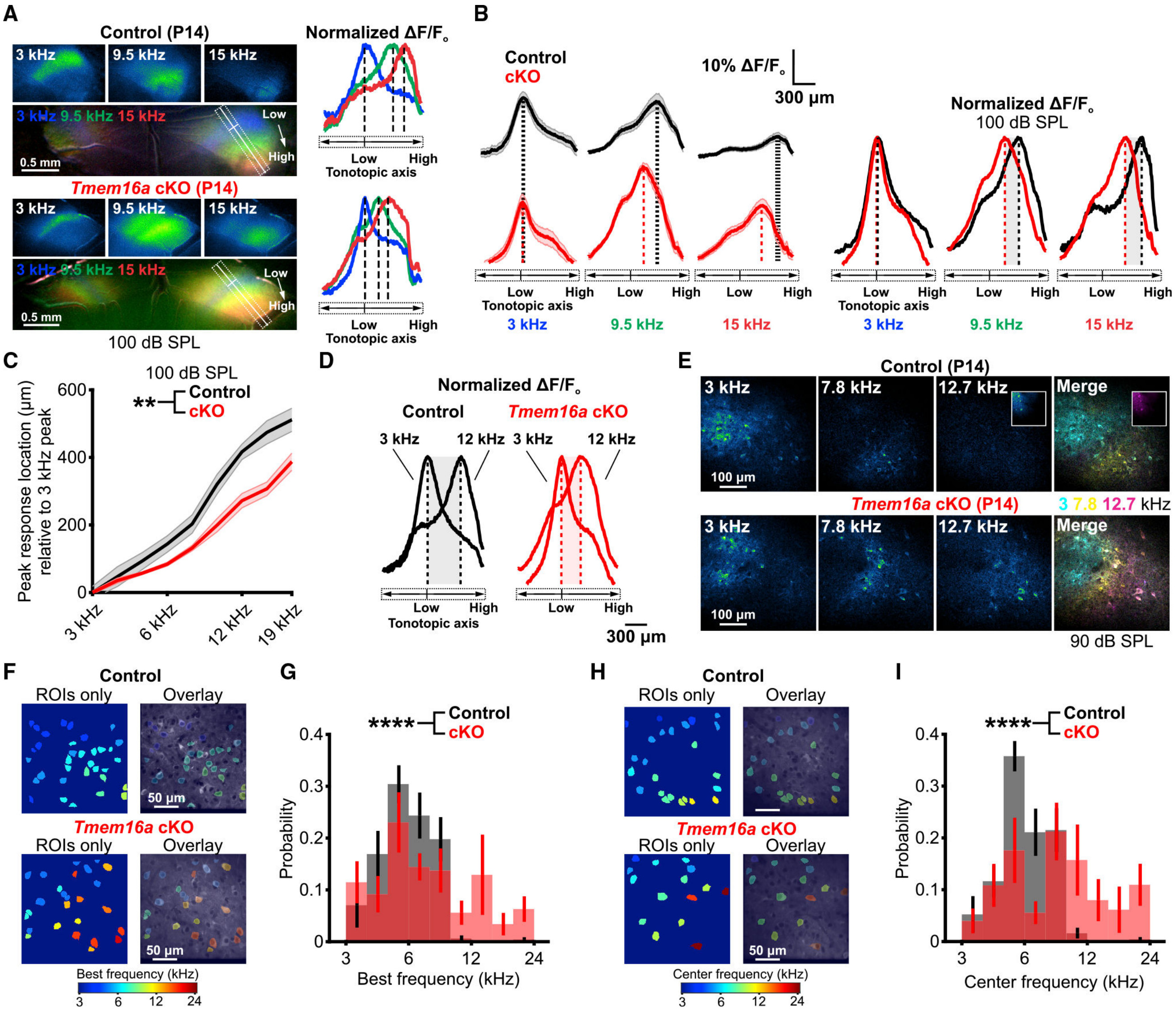

Figure 6. Spatial compression of frequency representation after disruption of developmental spontaneous activity

(A) Left: pseudocolored individual and merged images of tone-evoked neural calcium transients in P14 control (*Tmem16a$^{fl/fl}$;Snap25-T2A-GCaMP6s*) and P14 *Tmem16a* cKO (*Tecta-Cre;Tmem16a$^{fl/fl}$;Snap25-T2A-GCaMP6s*) mice. Rectangular ROIs were placed along the tonotopic axis of the contralateral IC (low to high frequency), perpendicular to pure-tone-evoked bands, to determine the peak response location. Right: plot of normalized pure-tone fluorescence response along the tonotopic axis for the animal at the left, with dashed lines indicating peak response location.

(B) Left: plot of mean tone-evoked fluorescence along the tonotopic axis of the IC in control (top) and *Tmem16a* cKO mice (bottom). A dashed line indicates the location of the peak response along the tonotopic axis. Right: normalized mean fluorescence along the tonotopic axis of the IC. Gray shading indicates a shift in peak response location between control and *Tmem16a* cKO mice. n = 9 control mice, 8 *Tmem16a* cKO mice, mean ± SEM.

(C) Quantification of peak response location relative to 3-kHz (lowest frequency) peak response location. n = 9 control mice, 8 *Tmem16a* cKO mice; mean ± SEM, p = 0.00540, linear mixed model.

(D) Plot of mean normalized tone-evoked fluorescence along the tonotopic axis of the IC to 3-kHz and 12-kHz pure tones. A dashed line indicates the peak response location, and shading indicates the difference between the 3-kHz and 12-kHz peak location. n = 9 control mice, 8 *Tmem16a* cKO mice.

(E) Low-magnification 2P imaging of tone-evoked neural activity in the IC of a P14 control and *Tmem16a* cKO mouse at a z depth of 150 μm. No 12.7-kHz-responsive cells were observed in the control field of view but were detected 150 μm laterally and 50 μm deeper than the field of view (inset). The pseudocolored merged image depicts spatial separation of tonal responses of neurons and neuropil.

(F) High-magnification 2P imaging of IC neuronal ROIs, pseudocolored by best frequency (BF), in a P14 control and *Tmem16a* cKO mouse.

(G) Histogram of BF distribution in a high-magnification IC field of view. n = 207 control cells (8 mice), 252 *Tmem16a* cKO cells (7 mice); p = 7.1869e–5, two-sample Kolmogorov-Smirnov test.

(H) High-magnification 2P imaging of IC neuronal ROIs, pseudocolored by center frequency (CF), in a P14 control and *Tmem16a* cKO mouse.

(I) Histogram of CF distribution in a high-magnification IC field of view. n = 207 control cells (8 mice), 252 *Tmem16a* cKO cells (7 mice); p = 1.1214e–10, two-sample Kolmogorov-Smirnov test.

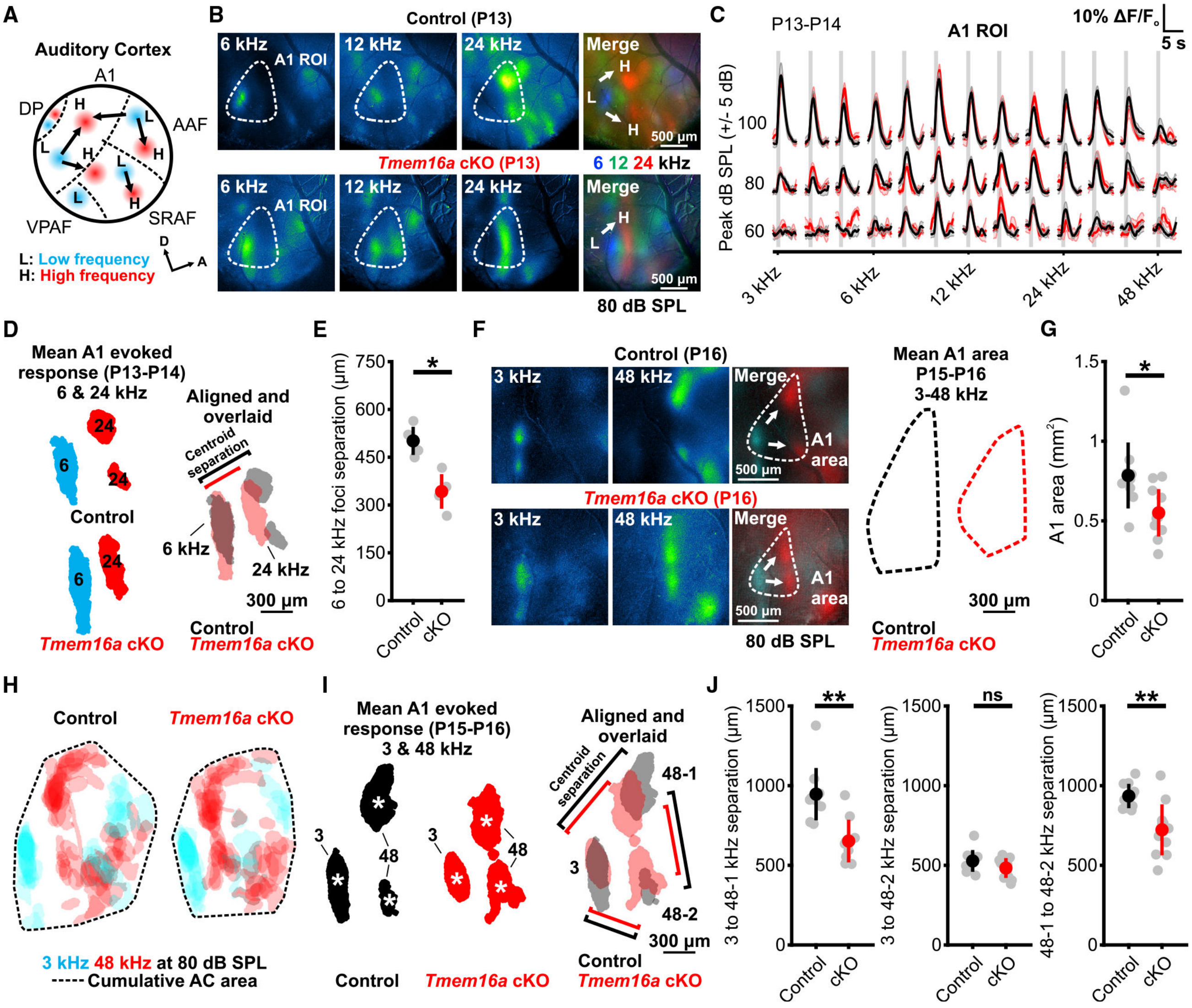

Figure 7. Disruption of pre-hearing spontaneous activity elicits spatial compaction of the AC

(A) Schematic depicting tonotopic organization of the mouse AC (adapted from Issa et al., 2014; Romero et al., 2020). L, low frequency; H, high frequency; A1, primary AC; AAF, anterior auditory field; SRAF, suprarhinal auditory field; VPAF, ventral posterior auditory field; DP, dorsal posterior.

(B) Tone-evoked neural calcium transients in the AC from P13 control (*Tmem16a*$^{fl/fl}$*;Snap25-T2A-GCaMP6s*) and P14 *Tmem16a* cKO (*Tecta-Cre;Tmem16a*$^{fl/fl}$*; Snap25-T2A-GCaMP6s*) mice at 80-dB SPL. The merged image shows tonotopic segregation of pseudocolored pure tone responses along tonotopic axes.

(C) Quantification of tone-evoked fluorescence in the A1 across a range of frequency and sound level stimuli in P13–P14 control and *Tmem16a* cKO mice. A vertical gray bar indicates tone presentation. n = 6 control mice, 6 *Tmem16a* cKO mice, mean ± SEM.

(D) Left: mean A1 evoked responses to 6-kHz (cyan) and 24-kHz (red) pure tones at 80-dB SPL in P13–P14 control and *Tmem16a* cKO mice. Right: mean 6- and 24-kHz pure tone responses from control and *Tmem16a* cKO mice aligned to the 6-kHz centroid and overlaid. Lines indicate mean centroid separation between low- and high-frequency foci.

(E) Quantification of centroid separation between 6- and 24-kHz foci. n = 4 control, 4 *Tmem16a* cKO mice; p = 0.0286, Wilcoxon rank-sum test.

(F) Left: tone-evoked neural calcium transients in the AC from a P16 control and *Tmem16a* cKO mouse at 80-dB SPL. The merged image shows the lower (3 kHz) and upper (48 kHz) bound locations of a frequency range in the A1. Right: mean A1 tone-responsive area activated by a 3- to 48-kHz frequency range. n = 10 control mice, 11 *Tmem16a* cKO mice.

(G) Quantification of mean A1 area. n = 10 control mice, 11 *Tmem16a* cKO mice; p = 0.0124, Wilcoxon rank-sum test.

(H) Cumulative tone responses in the AC of P15–P16 mice to 3-kHz and 48-kHz stimuli at 80-dB SPL. A black dashed line indicates the cumulative tone response area. n = 9 control, 10 *Tmem16a* cKO mice.

(I) Left: mean A1 evoked responses to 3-kHz and 48-kHz pure tones at 80-dB SPL in P15–P16 control and *Tmem16a* cKO mice. Centroids of pure tone foci are indicated by white asterisks. Right: mean 3- and 48-kHz pure tone responses from control and *Tmem16a* cKO mice aligned to the 3-kHz centroid and overlaid. Lines indicate mean centroid separation between low- and high-frequency foci.

(J) Quantification of centroid separation between low-frequency (3) and high-frequency (48–1 and 48–2) foci in the A1. n = 9 control, 10 *Tmem16a* cKO mice; p = 0.0044, 0.2875, 0.0065, Wilcoxon rank-sum test.

KEY RESOURCES TABLE

REAGENT or RESOURCE	SOURCE	IDENTIFIER
Antibodies		
Rabbit anti-MyosinVIIa, 25-6790	Proteus Biosciences	RRID: AB_10015251
Chicken anti-GFP, GFP-1010	Aves	RRID: AB_2307313
Rabbit anti-β3-tubulin, D71G9, #5568	Cell Signaling Tech	RRID: AB_10694505
Oligonucleotides		
Primer: cccagttgagattggaaagtg (Snap25GC6s-com-s)	Jackson Laboratory	N/A
Primer: acttcgcacaggatccaaga (Snap25GC6s-mut-as)	Jackson Laboratory	N/A
Primer: ctggttttgttggaatcagc (Snap25GC6s-wt-as)	Jackson Laboratory	N/A
Primer: GGCTCATCAATGTTCTGTTC (Tmem16a fl s)	Schreiber et al., 2015	N/A
Primer: CTCAAGTCCTCAAGTCCCAGTC (Tmem16a fl as)	Schreiber et al., 2015	N/A
Primer: gatggttgtggtgtgtctcg (Tecta-com-s)	Babola et al., 2020	N/A
Primer: cagtgatgagggaggaggtg (Tecta-WTas)	Babola et al., 2020	N/A
Primer: cctgtccctgaacatgtcca (Tecta-Mutas)	Babola et al., 2020	N/A
Additional oligonucleotides are listed in Table S1.		
Experimental models: Organisms/strains		
Mouse: B6.Cg-Snap25tm3.1Hze/J; Snap25-T2A-GCaMP6s	Jackson Laboratory	RRID: IMSR_JAX:025111
Mouse: B6.Cg-Tectaem1(icre)Dbe/J; Tecta-Cre	Dwight Bergles; Babola et al., 2020	RRID: IMSR_JAX:035552
Mouse: Gt(ROSA)26Sortm1.1(CAG-EGFP) Fsh/Mmjax; R26-lsl-EGFP	MMRRC	RRID: MMRRC_032037-JAX
Mouse: B6N; 129-Gt(ROSA) 26Sortm1(CAG-GCaMP3)Dbe/J; R26-lsl-GCaMP3	Dwight Bergles; Paukert et al., 2014	RRID: IMSR_JAX:028764
Mouse: Ano1tm1Jrr; TMEM16A-GFP	Jason Rock; Huang et al., 2012	MGI: 5442019
Mouse: Ano1tm1Bdh; Tmem16a fl	Jason Rock; Schreiber et al., 2015	MGI: 3809591
Software and algorithms		
MATLAB 2019b	Mathworks	RRID: SCR_001622
FIJI (ImageJ)	https://imagej.nih.gov/ij/	RRID: SCR_003070
CorelDRAW Graphics Suite	Corel	RRID: SCR_014235
RPvdsEX	Tucker-Davis Technologies	N/A
Custom analysis code	This manuscript	https://doi.org/10.5281/zenodo.7195670